Atmos. Chem. Phys., 12, 2149–2172, 2012
www.atmos-chem-phys.net/12/2149/2012/
doi:10.5194/acp-12-2149-2012

Atmospheric Chemistry and Physics

Seasonal observations of OH and HO_2 in the remote tropical marine boundary layer

S. Vaughan[1], T. Ingham[1,2], L. K. Whalley[1,2], D. Stone[1,3], M. J. Evans[3], K. A. Read[4,5], J. D. Lee[4,5], S. J. Moller[2,3], L. J. Carpenter[4], A. C. Lewis[4,5], Z. L. Fleming[6,7], and D. E. Heard[1,2]

[1]School of Chemistry, University of Leeds, Woodhouse Lane, Leeds, UK
[2]National Centre for Atmospheric Science, University of Leeds, Leeds, UK
[3]School of Earth and Environment, University of Leeds, Woodhouse Lane, Leeds, UK
[4]Department of Chemistry, University of York, York, UK
[5]National Centre for Atmospheric Science, University of York, York, UK
[6]Department of Chemistry, University of Leicester, Leicester, UK
[7]National Centre for Atmospheric Chemistry, University of Leicester, Leicester, UK

Correspondence to: D. E. Heard (d.e.heard@leeds.ac.uk)

Received: 23 June 2011 – Published in Atmos. Chem. Phys. Discuss.: 28 July 2011
Revised: 21 January 2012 – Accepted: 26 January 2012 – Published: 27 February 2012

Abstract. Field measurements of the hydroxyl radical, OH, are crucial for our understanding of tropospheric chemistry. However, observations of this key atmospheric species in the tropical marine boundary layer, where the warm, humid conditions and high solar irradiance lend themselves favourably to production, are sparse. The Seasonal Oxidant Study at the Cape Verde Atmospheric Observatory in 2009 allowed, for the first time, seasonal measurements of both OH and HO_2 in a clean (i.e. low NO_x), tropical marine environment. It was found that concentrations of OH and HO_2 were typically higher in the summer months (June, September), with maximum daytime concentrations of $\sim 9 \times 10^6$ and 4×10^8 molecule cm^{-3}, respectively – almost double the values in winter (late February, early March). HO_2 was observed to persist at $\sim 10^7$ molecule cm^{-3} through the night, but there was no strong evidence of nighttime OH, consistent with previous measurements at the site in 2007. HO_2 was shown to have excellent correlations ($R^2 \sim 0.90$) with both the photolysis rate of ozone, $J(O^1D)$, and the primary production rate of OH, $P(OH)$, from the reaction of $O(^1D)$ with water vapour. The analogous relations of OH were not so strong ($R^2 \sim 0.6$), but the coefficients of the linear correlation with $J(O^1D)$ in this study were close to those yielded from previous works in this region, suggesting that the chemical regimes have similar impacts on the concentration of OH. Analysis of the variance of OH and HO_2 across the Seasonal Oxidant Study suggested that ~70 % of the total variance could be explained by diurnal behaviour, with ~30 % of the total variance being due to changes in air mass.

1 Introduction

The hydroxyl radical, OH, is the dominant daytime oxidant in the troposphere. A major pathway for its formation is via the reactions

$$O_3 + h\nu(\lambda < 340\,\text{nm}) \rightarrow O(^1D) + O_2 \quad \text{(R1)}$$

$$O(^1D) + H_2O \rightarrow 2OH \quad \text{(R2)}$$

OH is closely coupled to the hydroperoxy radical, HO_2, so that they are often referred to collectively as the family HO_x (= OH + HO_2). The key process for the formation of HO_2 in this region is the reaction

$$OH + CO(+O_2) \rightarrow HO_2 + CO_2 \quad \text{(R3)}$$

which is also one of the main loss processes for OH in a clean environment. In the absence of NO, OH can then be reformed from HO_2 via the reaction

$$HO_2 + O_3 \rightarrow OH + 2O_2 \quad \text{(R4)}$$

Another important process for the removal of tropospheric OH is through its reactions with CH_4 and other volatile organic compounds (VOCs) to form peroxy radicals, RO_2

$$OH + CH_4, VOCs(+O_2) \rightarrow RO_2 + H_2O \quad \text{(R5)}$$

RO_2 can undergo self-reaction and ultimately form HO_2. For example, in the case of the methylperoxy radical, CH_3O_2,

$$CH_3O_2 + CH_3O_2 \rightarrow 2CH_3O + \text{other products} \quad \text{(R6)}$$

$$CH_3O + O_2 \rightarrow HO_2 + HCHO \quad \text{(R7)}$$

In environments where the levels of NO are very low, the concentration of HO_2 is controlled by the loss processes

$$HO_2 + HO_2 \rightarrow H_2O_2 + O_2 \quad \text{(R8)}$$

$$HO_2 + CH_3O_2 \rightarrow CH_3O_2H + O_2 \quad \text{(R9)}$$

HO_2 can also undergo heterogeneous loss with atmospheric aerosol, and this process has been shown to be important in the MBL (see, for example, Sommariva et al., 2004; Smith et al., 2006; Sommariva et al., 2006; Whalley et al., 2010). In environments with high concentrations of NO, the reactions

$$HO_2 + NO \rightarrow OH + NO_2 \quad \text{(R10)}$$

$$RO_2 + NO \rightarrow RO + NO_2 \quad \text{(R11)}$$

play an active role in the local chemistry. It is worth noting that the alkoxy radical, RO, generated in Reaction (R11) can react with O_2 to form HO_2, as in Reaction (R7).

It has also been shown that the reaction of HO_2 with halogen oxides, XO (where X = Br, I)

$$HO_2 + XO \rightarrow HOX + O_2 \quad \text{(R12)}$$

is significant in marine environments (Bloss et al., 2005b; Smith et al., 2006; Sommariva et al., 2006; Kanaya et al., 2007). The HOI and HOBr produced from Reaction (R12) can then either be removed through heterogeneous reaction with aerosol or photolysis to produce OH and a halogen atom, X. This halogen atom can then regenerate XO via the reaction

$$X + O_3 \rightarrow XO + O_2 \quad \text{(R13)}$$

Read et al. (2008) and Mahajan et al. (2010) showed that the inclusion of the chemistry of halogen oxides, present at only a few pptv, was vital in order for model simulations to reproduce their observations of ozone – the key precursor for OH in the remote MBL – at the Cape Verde Atmospheric Observatory (CVAO) in 2007.

The rate of primary production of OH from Reactions (R1) and (R2) is given by

$$P(\mathrm{OH}) = 2f[O_3] \times J(O^1D) \quad (1)$$

where $J(O^1D)$ is the photolysis rate of ozone and

$$f = \frac{k_{O^1D+H_2O}[H_2O]}{k_{O^1D+H_2O}[H_2O] + k_{O^1D+N2}[N_2] + k_{O^1D+O_2}[O_2]} \quad (2)$$

where the rate constants $k_{O^1D+H_2O}$ (2.1×10^{-10} cm^3 molecule^{-1} s^{-1}), $k_{O^1D+N_2}$ (3.1×10^{-11} cm^3 molecule^{-1} s^{-1}) and $k_{O^1D+O_2}$ (4.0×10^{-11} cm^3 molecule^{-1} s^{-1}) are for the respective reaction and quenching processes of O(^{1}D) (Atkinson et al., 2004) at $T \sim 298$ K, if all other removal processes for O(^{1}D) are insignificant. The rate of production of OH, in the absence of NO, can thus be defined as

$$\frac{d[\mathrm{OH}]}{dt} = P(\mathrm{OH}) + k_4[HO_2][O_3] + \sum_i v_i J_i[i] - \sum_n k_{\mathrm{OH}+L_n}[L_n][\mathrm{OH}] \quad (3)$$

where i represents the other photolytic processes that may lead to generation of OH (v_i is the stoichiometry of the process) and the last term is the total loss of OH to its sinks, such as the major reactions with CO and CH_4 and the minor contributions from reactions with other VOCs, such as acetaldehyde. For remote environments containing low concentrations of alkenes and other non-methane hydrocarbons, such as at the CVAO, the production of OH from the reaction of O(^{1}D) with water vapour has been shown to dominate the production of OH. Using the *Master Chemical Mechanism*, Whalley et al. (2010) performed a rate of production analysis for OH for this site and calculated that $P(\mathrm{OH})$ constitutes at least 75 % of the total rate of production of OH. Assuming that that the rate of OH production is dominated by $P(\mathrm{OH})$ leads to the following steady-state expression:

$$[\mathrm{OH}] = \frac{P(\mathrm{OH})}{\sum_n k_{\mathrm{OH}+n}[n]} = P(\mathrm{OH}) \times \tau_{\mathrm{OH}} \quad (4)$$

where τ_{OH} is the lifetime of OH with respect to its loss to all sinks. For a constant lifetime, a plot of [OH] against $P(\mathrm{OH})$ should be linear with slope τ_{OH}. This equation can also be rewritten in terms of $J(O^1D)$ as

$$[\mathrm{OH}] = (a \times J(O^1D)^b) + c \quad (5)$$

where a represents the influence of all chemical sources and sinks, b accounts for the effect of combining all photolytic processes that produce OH (i.e. photolysis of O_3 as well as NO_2, HOI, H_2O_2, etc.) into a single power function of $J(O^1D)$ (see Ehhalt and Rohrer, 2000), and c is the contribution from all light-independent processes. Equations (4) and (5) have been used successfully to explain the variability of OH in different chemical schemes (e.g. Creasey et al., 2002, 2003; Berresheim et al., 2003; Smith et al., 2006).

In the absence of NO, the rate of production of HO_2 is given by

$$\frac{d[HO_2]}{dt} = k_3[\mathrm{OH}][\mathrm{CO}] - 2k_8[HO_2]^2 - k_4[HO_2][O_3] - k_9[HO_2][CH_3O_2] \quad (6)$$

As the rate of Reaction (R4) is slow compared to Reactions (R8) and (R9), and the rate of loss of CH_3O_2 through reaction (R6) is slow compared to the rate of production, the steady-state concentration of HO_2 can be expressed as

$$[HO_2] = \sqrt{\frac{k_3[\mathrm{CO}][\mathrm{OH}]}{2k_5 + k_7\alpha}} = \sqrt{\frac{k_3[\mathrm{CO}]}{2k_5 + k_7\alpha}} \times \sqrt{P(\mathrm{OH}) \times \tau_{\mathrm{OH}}} \quad (7)$$

where α = $[CH_3O_2]/[HO_2]$. For constant values of [CO], α and τ_{OH}, a plot of $[HO_2]$ against $\sqrt{P(OH)}$ should be linear.

As can be seen in Eqs. (1) and (2), the rate of production of OH is controlled by the concentration of water vapour and $J(O^1D)$. Thus, the high solar irradiance and the warm, humid conditions in the tropics lend themselves favourably to OH generation. OH can then react rapidly with the many trace VOCs found in the troposphere, initiating their oxidation and, ultimately, the removal of these species from the atmosphere. This process is of particular importance when considering the role of OH in constraining the atmospheric budget of methane, the third most abundant greenhouse gas and second only to CO_2 of the long-lived greenhouse gases in terms of radiative forcing (Forster et al., 2007). Lawrence et al. (2001) used a global model to estimate that ∼75 % of atmospheric methane is oxidized between 30° N and 30° S. Bloss et al. (2005a) used the GEOS-CHEM model to estimate that 80 % of methane is removed in the tropical troposphere through OH-initiated oxidation, with as much as 25 % of the total occurring in the MBL. Therefore, reliable measurements of OH in tropical areas are of crucial importance for understanding the global oxidizing capacity of the troposphere and future climate change.

Simultaneous measurements of OH and HO_2 in the tropical boundary layer are still relatively sparse compared to the number of studies at mid-latitudes in the Northern Hemisphere, for example (see Heard and Pilling, 2003, and references therein). In recent years, the number of measurement campaigns in the tropics has increased, and Table 1 provides a brief summary of the results of previous studies in tropical and remote MBL regions. Ground-based measurements of OH have been made at the Mauna Loa Observatory in Hawaii (Tanner and Eisele, 1995; Hoell et al., 1996; Eisele et al., 1996), although that station is ∼3.5 km above sea level and, as such, the conditions are closer to free tropospheric than typical of the boundary layer. Airborne measurements of HO_x were made during the Pacific Exploratory Missions (PEM) (Hoell et al., 1999; Mauldin et al., 1999; Raper et al., 2001; Tan et al., 2001; Mauldin et al., 2001) and the Transport and Chemical Evolution over the Pacific (TRACE-P) campaign (Jacob et al., 2003; Mauldin et al., 2003; Cantrell et al., 2003; Olson et al., 2004), but measurements in the tropical boundary layer in both studies were limited. HO_x-measurements have also been made over the tropical Atlantic Ocean and the pristine Amazon rainforests of Suriname, Guyana and French Guiana (Lelieveld et al., 2008); on two separate campaigns in the Mexico City Metropolitan Area (Shirley et al., 2006; Dusanter et al., 2009a); at the Pearl River Delta, China (Hofzumahaus et al., 2009); over Western Africa as part of the African Monsoon Multidisciplinary Analyses (AMMA) campaign (Commane et al., 2010; Stone et al., 2010); and in Malaysian Borneo as part of the Oxidant and Particle Photochemical Processes (OP3) project (Hewitt et al., 2010; Pugh et al., 2010; Whalley et al., 2011; Stone et al., 2011a). However, these studies were predominantly in or over either forested or polluted regions, so that the chemistry of HO_x was heavily influenced by processes other than Reactions (R1)–(R12). There have been several studies in the remote MBL outside of the tropics – for example, at Cape Grim, Tasmania, as part of the Southern Ocean Photochemistry Experiment (SOAPEX-2) (Creasey et al., 2003), and on remote Japanese islands (see Kanaya and Akimoto, 2002 and the references therein; Kanaya et al., 2007). However, measurements of OH and HO_2 in the remote tropical MBL are still very limited. Concentrations of OH were measured using Differential Optical Absorption Spectroscopy (DOAS) onboard the R/V Polarstern in the tropical Atlantic as part of the Air Chemistry and Lidar Studies of Tropospheric and Stratospheric Species on the Atlantic Ocean (ALBATROSS) project in late 1996 (Brauers et al., 2001). In that study, it was found that OH followed a clear diurnal cycle, with maximum concentrations of about 7×10^6 molecule cm^{-3} at local noon, within the range observed above the tropical Pacific during the PEM. Also, [OH] and $[HO_2]$ was measured by Whalley et al. (2010) at the CVAO as part of the Reactive Halogens in the Marine Boundary Layer Experiment (RHaMBLe) in 2007 – the maximum daytime concentrations of OH and HO_2 were 9×10^6 and 6×10^8 molecule cm^{-3}, respectively.

Almost all these studies of HO_x have been "short-term"; i.e. the observation periods are typically of the order of a few weeks at one particular period of the year. For example, the measurements of Whalley et al. (2010) at the CVAO were conducted over just 11 days, with only 5 days of OH data. To date, there has been only one long-term observational study of the seasonal change in [OH] in the troposphere (Rohrer and Berresheim, 2006), a five-year dataset measured at the Meteorological Observatory Hohenpeissenberg (MOHp; 47.8° N, 11.0° E) at ∼1000 m above sea-level in rural southern Germany. However, there have been no studies of seasonal trends in [OH] in the tropics where the levels of H_2O vapour and $J(O^1D)$ are strongly favourable for its formation and critical for constraining atmospheric methane. To that purpose, measurements of OH and HO_2 were performed at the CVAO as part of the Seasonal Oxidant Study (SOS) during three distinct periods of 2009: 27 February–8 March (SOS1), 6–16 June (SOS2) and 1–15 September (SOS3). This paper reports the observations of OH and HO_2 from this study and their respective dependencies on $J(O^1D)$ and $P(OH)$. The results are compared with the previous measurements made at the same site by Whalley et al. (2010) and with other tropical locations, and the seasonal variability will be discussed.

Table 1. Summary of measurement campaigns of HO_x in tropical and remote marine regions; studies that included measurements in the tropical MBL are shown in bold.

Campaign	Location	Environment	Platform	HO_x	Comments	Reference
PEM-Tropics A	**Pacific Ocean 30° N–30° S 75–165° W**	**Marine**	**Aircraft**	**$[OH]_{midday}$=6–8×10^6 molecule cm^{-3} in boundary layer**	**Mainly higher altitudes (i.e. above 2 km). Dry season.**	**Hoell et al. (1999) Mauldin et al. (1999)**
OKIPEX	Oki Dogo Island, Japan 36.3° N, 133.2° E	Clean marine	Ground	$HO_{2,peak}$ ∼9 pptv $HO_{2,night}$ ∼0–3 pptv	Good agreement between model and daytime HO_2 for some days, factor of 2 difference other days.	Kanaya et al. (1999) Kanaya et al. (2000)
ALBATROSS	**Atlantic Ocean 5° N–37° S, 26–36° W**	**Clean marine**	**Ship**	**up to [OH]∼10^7 molecule cm^{-3} in clean air**	**Model overpredicts OH by 16 %**	**Brauers et al. (2001)**
ORION99	Okinawa Island, Japan 26.9° N, 128.3° E	Clean marine	Ground	$[OH]_{peak}$ ∼4×10^6 molecule cm^{-3} $HO_{2,peak}$ ∼17 pptv $HO_{2,night}$ ∼2–5 pptv	$[HO_2]$:[OH]∼76; model underestimated daytime HO_2 by ∼20 % and cannot reproduce nighttime HO_2	Kanaya et al. (2001a) Kanaya et al. (2001b)
PEM-Tropics B	**Pacific Ocean 36° S–38° N 76° E–148° W**	**Marine**	**Aircraft**	**$[OH]_{midday}$=6–8×10^6 molecule cm^{-3} in boundary layer (CIMS)**	**FAGE showed good agreement during intercomparison flight. Wet season.**	**Raper et al. (2001) Mauldin et al. (2001) Eisele et al. (2001)**
			Aircraft	**OH_{mean}∼0.1 pptv (<2 km) $HO_{2,mean}$∼10 pptv (<2 km)**	**Low altitudes – model overpredicts OH and HO_2; HO_x predicted to be larger in spring than autumn; OH seasonal changes due to changes in $[O_3]$, $[H_2O]$ and $J(O^1D)$**	**Tan et al. (2001) Davis et al. (2001) Olson et al. (2001)**
RISOTTO 1999–2000	Rishiri Island, Japan 45.1° N, 141.1° E	Clean marine, semi-forested	Ground	$HO_{2,peak}$ ∼10 pptv $HO_{2,night}$ ∼0–8 pptv	Model underpredicts nighttime HO_2 and overpredicts daytime HO_2 by ∼70 %, but inclusion of iodine chemistry improves agreement.	Kanaya et al. (2002a, b)
SOAPEX-2	Cape Grim, Tasmania 40.7° S, 144.7° E	Clean marine, semi-polluted and polluted	Ground	$[OH]_{peak}$=3.5×10^6 molecule cm^{-3} $[HO_2]_{peak}$=2×10^8 molecule cm^{-3}	Good correlations between concentrations of both OH and HO2 with $J(O^1D)$, $P(OH)$. Steady-state calculations overestimate [OH] in clean air by 20 %.	Creasey et al. (2003)
TRACE-P	**Pacific Ocean 14–33° N 137.5° E–146° W**	**Marine**	**Aircraft**	**HO_2 up to 30 pptv (<1 km) OH up to 0.4 pptv (<1 km)**	**HO_2 overpredicted and OH underestimated at low altitudes. Discrepancy of ∼50 % in intercomparison measurements of OH and HO_2 between two instruments on different aircraft.**	**Jacob et al. (2003) Mauldin et al. (2003) Cantrell et al. (2003) Eisele et al. (2003) Olson et al. (2004)**
MCMA2003	Mexico City 19.4° N, 99.1° W (2.2 km altitude)	Urban polluted	Ground	$[OH]_{peak}$=8–13×10^6 molecule cm^{-3} $[HO_2]_{peak}$=5–20×10^8 molecule cm^{-3} $HO_{2,night}$=0.8–32 pptv	strong HO_x scavenging during rush hour; τ_{OH} ∼120 s^{-1}; typical $[HO_2]$:[OH]∼120; values of [OH] and $[HO_2]$ reported here have been adjusted by factor of 1.6 from those reported in Shirley et al. (2006) as recommended by Mao et al. (2010)	Shirley et al. (2006)

Table 1. Continued.

Campaign	Location	Environment	Platform	HO_x	Comments	Reference
–	Rishiri Island, Japan 45.1° N, 141.1° E	Clean marine, semi-forested	Ground	$[OH]_{peak}$ ~2.7×10^6 molecule cm^{-3} $HO_{2,peak}$ ~5.9 pptv $[OH]_{night}$=(0.7–5.5) $\times10^6$ molecule cm^{-3} $HO_{2,night}$ ~0.5–4.9 pptv	Model overpredicts by 89 % and 35 % daytime HO_2 and OH, respectively.	Kanaya et al. (2007)
GABRIEL	**Amazon forest Atlantic Ocean 3–6° N, 50–60° W**	**Marine and forested**	**Aircraft**	**$[OH]_{mean,ocean}=9.0\times10^6$ molecule cm^{-3} $[OH]_{mean,forest}=5.6\times10^6$ molecule cm^{-3} $[HO_2]_{mean,ocean}=6.7\times10^8$ molecule cm^{-3} $[HO_2]_{mean,forest}=10.5\times10^8$ molecule cm^{-3}**	**Boundary layer concentrations; results suggest recycling of HO_x over forest through oxidation of isoprene**	**Lelieveld et al. (2008) Martinez et al. (2008)**
MCMA2006 MILAGRO	Mexico City 19.4° N, 99.1° W (2.2 km altitude) (different site to MCMA2003)	Urban polluted	Ground	$[OH]_{peak}$=2–15×10^6 molecule cm^{-3} median $[OH]_{peak}$ ~5×10^6 molecule cm^{-3} $[HO_2]_{peak}$=0.6–6.5×10^8 molecule cm^{-3} median $[HO_2]_{peak}$ ~2×10^8 molecule cm^{-3}	average diurnal HO_2 peaks one hour after OH; [OH] correlates poorly with $J(O^1D)$ and J(HONO); $[HO_2]$:[OH] lower than in 2003; model underestimates both [OH] and $[HO_2]$	Dusanter et al. (2009a, b)
INTEX-B	**Mexico City and Pacific Ocean 15–65° N, 90–170° W**	**Urban polluted and marine**	**Aircraft**	**OH_{median} up to 0.2 pptv (<2 km) $HO_{2,median}$ up to ~15 pptv <(2 km)**	**Simultaneous with MILAGRO; levels of OH and HO_2 overpredicted by model below 2 km**	**Mao et al. (2009) Singh et al. (2009) Emmons et al. (2010)**
PRiDE-PRD2006	Pearl River Delta, China 23.5° N, 113.0° E	Rural polluted	Ground	average diurnal peak values $[OH]_{peak}=13\times10^6$ molecule cm^{-3} $[HO_2]_{peak}=17\times10^8$ molecule cm^{-3}	Model severely underpredicts OH and HO_2 => regeneration pathway independent of NO	Hofzumahaus et al. (2009)
AMMA	**West Africa 4–18° N, 8° W–4° E**	**Marine and forested**	**Aircraft**	**OH~0.2 pptv HO_2~15 pptv**	**Median mixing ratios at ≤0.5 km; $[HO_2]$:[OH]~80; up to 10 pptv of HO_2 observed at night; model gives good agreement for HO_2 but overestimates OH by factor of 2.5**	**Commane et al. (2010) Stone et al. (2010)**
RHaMBLe	**Cape Verde Atmospheric Observatory 16.9° N, 24.8° W**	**Remote marine**	**Ground**	**$[OH]_{peak}=9\times10^6$ molecule cm^{-3} $[HO_2]_{peak}=6\times10^8$ molecule cm^{-3} HO_2~0.6 pptv measured on two nights**	**Good agreement with model predictions, especially for OH; $[HO_2]$ strongly dependent on aerosol losses**	**Whalley et al. (2010)**

Table 1. Continued.

Campaign	Location	Environment	Platform	HO_x	Comments	Reference
OOMPH	Atlantic Ocean 28–57° S, 46° W–34° E	Remote marine	Ship	$[OH]_{peak} \sim 6\times10^6$ molecule cm^{-3} $HO_{2,peak} \sim 15$ pptv	Good agreement with simple steady-state model for both species	Hosaynali Beygi et al. (2011)
OP3	Danum Valley, 5.0° N, 117.8° E (425 m a.s.l.)	Forested	Ground	average diurnal peak value $[OH] \sim 2\times10^6$ molecule cm^{-3} $[OH]_{max} = 7.2\times10^6$ molecule cm^{-3}	Model overpredicts HO_2 and underpredicts OH	Whalley et al. (2011)
	Malaysian Borneo 4–7° N,114–120° E	**Marine and forested**	**Aircraft**	**$[OH]_{mean}$=2.3×10^6 molecule cm^{-3} $[HO_2]_{mean}$=3.3×10^8 molecule cm^{-3}**	**Boundary layer (<2 km)**	**Stone et al. (2011)**
NAMBLEX	Mace Head, Ireland 53.32° N, 9.90° W	Remote marine	Ground	Range of noon-values $[OH]_{max}$ = 3–8 × 10^6 molecule cm^{-3} $[HO_2]_{max}$ = 0.9–2.1 × 10^8 molecule cm^{-3}	Significant influence of halogen oxide chemistry on HO_2 concentrations	Smith et al. (2011) Sommariva et al. (2006)

2 Experimental

2.1 Measurement of OH and HO_2 radicals

Fluorescence Assay by Gas Expansion (FAGE) has been well-demonstrated as a powerful tool for atmospheric measurements of HO_x (Heard and Pilling, 2003). OH and HO_2 were monitored at the CVAO using the University of Leeds' aircraft-FAGE instrument in a ground configuration. The instrument has been described elsewhere (Commane et al., 2010), but a brief description will be provided here. The instrument sampled ambient air through a pinhole and the gas flowed through detection cells for OH and HO_2 in series. The laser-induced on-resonance fluorescence following excitation of the transition $A^2\Sigma^+(v'=0) \leftarrow X^2\Pi_i\ (v''=0)$ $Q_1(2)$ of OH at $\lambda = 308$ nm was used as the basis for the detection of the hydroxyl radical. A reference cell, containing a heated filament used to thermally decompose water vapour to yield OH, was used to identify the wavelength at which the fluorescence of OH at that transition was greatest. Between the two detection cells was an injection port for NO, so that HO_2 is chemically converted to OH, which is subsequently detected at $\lambda \sim 308$ nm. The instrument was run at a low internal pressure (typically, $P = 2.2$ Torr) in order to reduce the effect of quenching on the fluorescence lifetime of OH and scattering of the laser light. This methodology allowed the use of temporal gating of the detector, a channel photomultiplier (CPM; Perkin-Elmer C943P), so that the fluorescence could be discriminated from the laser pulse. The CPM was gated off until ∼110 ns after the laser pulse (full-width half-maximum = 35 ns) to avoid detector saturation. Note that an in-house computer program automatically corrected the timing of the CPM-gates for any changes in the timing of the laser pulse. Photons from fluorescence and scattered light were then recorded using a two-channel gated photon counter. The first gate (Gate A, width 1 µs) recorded both fluorescence and background light (laser, solar and dark counts). The second gate (Gate B, width 20 µs) was set to switch on beyond the lifetime of the fluorescence at a delay of 5 µs and hence counted only background light (solar and dark counts). Summing over 1 s, the signal (count s^{-1}) due to fluorescence and laser scatter was calculated as signal A – (signal B/20). The laser scatter was removed from that signal by subtracting the observed signal when the laser is tuned off the OH resonance. Typically, 300 online and 60 offline one-second data points were collected for OH. Scanning the laser wavelength to the peak OH transition at the beginning of each measurement cycle typically took ∼120 s, so that each measurement cycle lasted usually about 540 s. Because the HO_2 detection will inherently observe OH from the sampled ambient air as well as that generated in situ from chemical conversion of HO_2 to OH, the injection of NO started 60 s after the instrument began recording online fluorescence signals, and that signal was subtracted from the subsequent signal with NO flowing to give only the signal due to converted

HO_2. Thus, there are typically 240 online and 60 offline one-second data points for HO_2. The fluorescence signals are then normalised with respect to the laser power entering each detection cell (typically 10–30 mW in the OH cell, 3–6 mW in the HO_2 cell).

The observed fluorescence signal, S_{OH} (count s^{-1} mW^{-1}), were related to [OH] by

$$S_{OH} = C_{OH} \times [OH] \quad (8)$$

where C_{OH} is the sensitivity of the instrument (count s^{-1} mW^{-1} $molecule^{-1}$ cm^3) with respect to OH and can be defined empirically by the expression

$$C_{OH} = D \times T_{OH} \times f_{gate} \times \Phi_f \quad (9)$$

where D is a function of pressure-independent parameters (e.g. laser power, collection efficiency of the optics, quantum yield of detector), T_{OH} is the transmission of OH within the instrument, f_{gate} is the fraction of light sampled within the timing gate and Φ_f is the fluorescence quantum yield from excited OH. The equations linking S_{HO_2}, C_{HO_2} and [HO_2] are analogous to Eqs. (8)–(9). The sensitivity at a given cell pressure and water vapour concentration was calibrated by measuring the observed fluorescence of OH and HO_2 generated in a flow of air from the photolysis of a known concentration of water vapour at $\lambda = 184.9$ nm (see Commane et al. (2010) for more details). Calibrations were performed regularly under the same conditions (i.e. laser power, instrument pressure) as for ambient sampling when possible and verified in the laboratory after the campaign.

The mixing ratio of ambient water vapour during the measurement periods (2–3 %) was greater than could be achieved in a field calibration (∼1.2 %). Hence, the calibrated sensitivities were corrected for the quenching of the OH fluorescence by water vapour using known rate parameters that contribute to the terms f_{gate} and Φ_f

$$f_{gate} = e^{-\Gamma t_1} - e^{-\Gamma t_2} \quad (10)$$

$$\Phi_f = \frac{\tau^{-1}}{\Gamma} \quad (11)$$

where τ is the radiative lifetime of the excited OH state ($A^2\Sigma^+$) in the absence of quenchers (688 ns; German, 1975), Γ is the total rate of removal of excited OH via radiative and quenching processes (calculated using the quenching rate constants of N_2, O_2 and water vapour at $T \sim 293$ K reported in Bailey et al. (1997) and Bailey et al., 1999) and t_1 and t_2 are the start and cut-off times for the photon-sampling gates, respectively. By comparing the relative values of f_{gate} and Φ_f for the conditions of the calibration and atmospheric sampling, one can correct the sensitivity of the instrument to OH and HO_2. These corrections lowered the instrument sensitivity by 10–30 %, raising the calculated [OH] and [HO_2] by the same relative proportion. The quenching-corrected instrument sensitivity (ct s^{-1} mW^{-1} $molecule^{-1}$ cm^3) with respect to OH was found to decrease through SOS, from $\sim 1.5 \times 10^{-7}$ to $\sim 0.6 \times 10^{-7}$, possibly because of reduced transmission of OH through the instrument or contamination/aging of the optics. The uncorrected sensitivity towards HO_2 was generally consistent at $\sim 1.9 \times 10^{-7}$ ct s^{-1} mW^{-1} $molecule^{-1}$ cm^3 throughout the campaigns, but increasing concentrations of water vapour from SOS1–3 led to effective instrument sensitivities (ct s^{-1} mW^{-1} $molecule^{-1}$ cm^3) of $\sim 1.8 \times 10^{-7}$ in SOS1 to $\sim 1.3 \times 10^{-7}$ in SOS3. Recent work by Fuchs et al. (2011) has highlighted a possible interference towards HO_2-detection by LIF from the chemical conversion of alkene- and aromatic-derived peroxy radicals to OH by NO which is added inside the fluorescence cell, with alkane-derived peroxy radicals exhibiting negligible interference. The concentrations of alkenes such as ethene and propene at the CVAO have been observed to be only a few pptv (see Carpenter et al. (2010) and Table 2). It is therefore expected that peroxy radicals derived from such alkenes generate only a very small HO_2 interference. Calculations using a box model incorporating the full *Master Chemical Mechanism* and constrained using the VOC measurements at the site (Table 2) show that ∼90 % of the RO_2 species are HO_2 and CH_3O_2, with other significant species being $CH_3C(O)O_2$ (5 %) and $C_2H_5O_2$ (0.9 %), all of which showed no HO_2 interference during laboratory experiments. The RO_2 species $OHC_2H_4O_2$ (0.6 % of RO_2 total) and $OHC_3H_6O_2$ (0.6 %), derived from ethene and propene, respectively, do give some HO_2 interference (measured in the laboratory as 40 % with the experimental configuration used here), but their very low abundance leads to only a very small HO_2 interference. However, for other environments, such as forested or urban, where the concentrations of alkenes and aromatics may be considerably higher, HO_2 interferences from such RO_2 species may need to be taken into account.

The limits of detection (LOD) of OH and HO_2, were defined as

$$\mathrm{LOD} = \frac{S/N}{C \cdot P} \cdot \sqrt{\left(\frac{1}{m} + \frac{1}{n}\right)} \cdot \sigma_b \quad (12)$$

where S/N is the signal-to-noise ratio (taken as 1 for both species), C is the instrument sensitivity, P is the laser power (mW), m is the number of online 1 s samples (typically 300 for OH and 240 for HO_2), n is the number of 1 s offline samples (generally 60 for both species) and σ_b is the standard deviation of the offline signal (ct s^{-1}) calculated using Poisson statistics and includes the contributions due to solar scatter, laser scatter and dark counts. The limits of detection of OH (five-minute averaging) and HO_2 (four-minute averaging) over the whole SOS were in the ranges (2–11) $\times 10^5$ and (6–13) $\times 10^5$ molecule cm^{-3}, respectively. A range of LODs was observed for both species because of the variability in both the offline signal and the quenching-corrected sensitivities across the whole SOS period. The uncertainty (2σ) in the measurements of [OH] and [HO_2] can be calculated as

Table 2. Summary of the mean and standard deviations of NO, NO_2, NO_y, CO, O_3 and VOCs at the CVAO during the HO_x-measurement periods of SOS1 and 2. Note that the NO, NO_2 and NO_y data coverage was sporadic across these periods.

Species	Detection limit	SOS1 (28 Feb–8 Mar)	SOS2 (6–16 Jun)
NO/pptv	1.5	9.2 ± 9.3	11 ± 17
NO_2/pptv	4.1	37 ± 56	no measurements
NO_y/pptv	3.4	562 ± 107	250 ± 73
CO/ppbv	3	114 ± 8	88 ± 7
O_3/ppbv	0.05	41 ± 5	23 ± 5
ethane/pptv	2.6	1473 ± 306	581 ± 122
ethene/pptv	2.8	51 ± 21	32 ± 19
propane/pptv	1.7	341 ± 140	35 ± 33
propene/pptv	1.6	16 ± 4	11 ± 2
i-butane/pptv	1.2	32 ± 18	3.3 ± 1.9
n-butane/pptv	1.2	54 ± 34	3.8 ± 2.1
acetylene/pptv	2.4	136 ± 34	44 ± 9
but-1-ene/pptv	1.5	7 ± 1	5 ± 1
i-pentane/pptv	0.9	9 ± 8	0.9 ± 1.4
n-pentane/pptv	0.7	9 ± 6	1.4 ± 1.4
hexane/pptv	0.7	2.1 ± 1.8	0.1 ± 0.4
isoprene/pptv	0.9	0.4 ± 0.8	0.04 ± 0.22
benzene/pptv	1.0	44 ± 15	9 ± 2
toluene/pptv	0.9	199 ± 560	0.04 ± 0.21
acetaldehyde/pptv	17.6	1142 ± 383	573 ± 177
methanol/pptv	7.0	690 ± 623	286 ± 107
acetone/pptv	2.8	1102 ± 667	473 ± 50

the square root of the sum of squares of the errors in the contributing variables, and was estimated to be ∼32 % for both species.

The CVAO is located on the island of Sao Vicente (16.86° N, 24.87° W), approximately 10 m above sea level and about 50 m from the coastline; a full description of the site is given in Carpenter et al. (2010). Levels of NO are typically a few pptv (Lee et al., 2009), so the observatory is an ideal location for monitoring atmospheric composition in a clean, remote tropical MBL. The laser system and data-acquisition electronics were located inside an air-conditioned standard shipping container. The sampling inlet of the instrument was on the roof of this container inside an insulated aluminium box, to protect against sea salt and water. To reduce the amount of scattered light detected, and also improve the transmission of OH and HO_2 through the instrument, a tube made of black nylon was placed inside the inlet between the sampling pinhole and the detection cell for OH, thus improving both the sensitivity of the instrument and the limit of detection.

2.2 Ancillary measurements

The photolysis rate of ozone to produce $O(^1D)$, $J(O^1D)$, was measured using a 2π-filter radiometer mounted on the roof of the container, about 2 m from the FAGE inlet, and was at no time in the shade of local influences (e.g. other instruments or structures at the CVAO). The signal from the radiometer was recorded as a voltage on the PC used to control the FAGE instrument and was later converted to a photolysis rate (s^{-1}) using the parameters (including factors to correct for solar zenith angle, ozone column density and temperature) obtained during the intercomparison study in Julich (Bohn et al., 2008). These data showed almost 1:1 agreement (slope = 1.02; $R^2 = 0.97$) with the output of the University of Leicester's spectral radiometer, which was positioned within a few metres at the same altitude, when the two radiometers were running simultaneously during SOS3.

Other ancillary measurements were made at the site, including those of NO_x (i.e. NO and NO_2), CO, O_3, VOCs (including short-chain alkanes and alkenes, acetaldehyde, acetone, methanol), relative humidity and wind direction, to allow characterisation of the atmospheric composition at the site. The majority of these measurements are part of a long-term dataset that has been running since 2006. Further details of the relevant instrumentation can be found in Carpenter et al. (2010). Table 2 shows average measured values and standard deviations of important species for the periods with simultaneous measurements of OH and HO_2 during SOS1 and 2.

2.3 Analysis of the data

The data were filtered for unfavourable meteorological conditions (e.g. heavy rainfall, as experienced during SOS3) and obvious influence of local pollution sources. Figure 1 shows examples of how pollution sources, such as the site power generator or passing fishing boats, distort the HO_2:OH ratio on short timescales because of the conversion of HO_2 to OH by NO. Data were filtered out if the concurrent wind direction and speed data suggested that the sampled air mass was from an obviously polluted source, such as generator exhaust fumes. The fast (i.e. 1 s) NO_x data would be required to allow identification of short pollution episodes from other sources, such as fishing boats; unfortunately, that data were not available for the bulk of the HO_x-measurement period. The predominant wind direction was NE from the open Atlantic ocean (∼94 % of the time), with the generator located southerly to the HO_x-instrument, so the wind direction (i.e. between 100° and 300°) could be used to identify data affected by local pollution influences and then removed from the final analysis.

The OH- and HO_2-signals were corrected for any instability in the wavelength of the laser; the full-width half-maximum of the $Q_1(2)$ transition at $\lambda = 308$ nm is very narrow (calculated using the procedure described in Dorn et al. (1995) to be less than 1 pm at $P \sim 2$ Torr), so that the magnitude of the fluorescence is highly sensitive to the incident wavelength. Figure 2 shows two examples of the HO_2-signals (black lines) as well as the corresponding values of the scaled reference signal (red). Note that laser

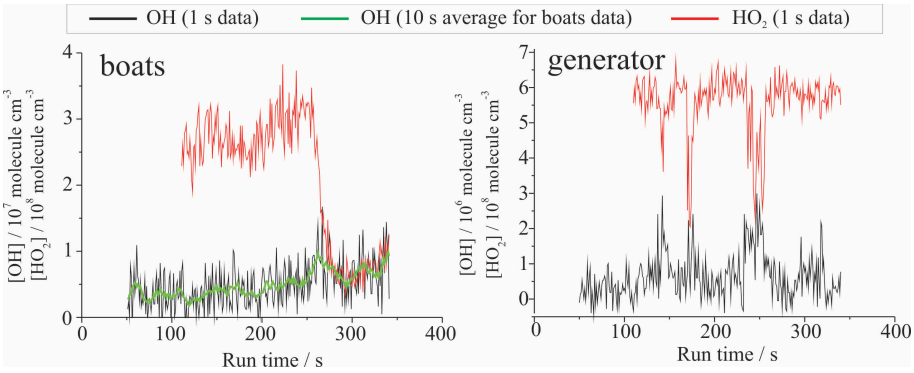

Fig. 1. [OH] (black) and [HO_2] (red) recorded at 1 Hz showing influences of pollution from passing boats on 16 June 2009 (left) and the site power generator on 5 September 2009 (right); the green line in the left-hand panel is the 10 s running average of the OH data. The HO_2 data in the right-hand panel have been offset by $+2 \times 10^8$ molecule cm^{-3} for clarity.

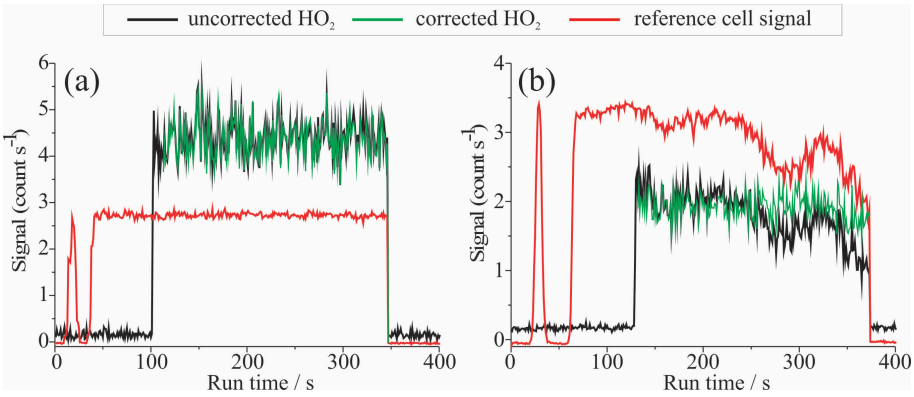

Fig. 2. Plots showing two examples of measured HO_2 signals (black line) without **(a)** and with **(b)** significant variation in the laser wavelength, observed as the response of the scaled reference cell signal (red line). The corrected HO_2-signals are represented by the green lines.

power, instrument and reference cell pressures and $J(O^1D)$ were constant (albeit for instrument noise) within each run and the early peaks in the reference signal correspond to where the laser wavelength was scanned to find the maximum of the OH fluorescence. Figure 2a shows a run where the laser wavelength appears to be stable, as can be seen by the flat profile of the reference signal after ∼100 s. Figure 2b clearly shows that the HO_2 signal appeared to follow the same pattern as the reference signal, such that the linear correlation between the two signals was reasonably strong ($R^2 = 0.80$). Because there was no evidence of significant changes in $J(O^1D)$, laser power or the pressures inside the instrument and the reference cell, this effect was most likely as a result of small fluctuations in the laser wavelength. By normalising the OH- and HO_2-signals to the reference signal, one is able to correct for the small variations in λ, as can be seen by the green line in Fig. 2b. A similar correction applied to the data in panel (a) suggested little change. Thus, this correction for small changes in wavelength, applied to the raw signals for both species, allowed data to be included in the analysis that may have otherwise been excluded.

3 Results

3.1 Summary of data and synoptic conditions

There were 33 days of OH and HO_2 observations, made in three intensive periods over seven months, constituting 500 014 and 413 205 one-second data points for OH and HO_2, respectively. Figures 3–5 show the time-series for each of the three campaigns. The shaded areas in the top panels represent the contributions to the air mass from five possible sources, as calculated using the NAME dispersion model (Ryall et al., 2001) using the technique described in detail in Carpenter et al. (2010) – Atlantic continental air from over North America (yellow), Atlantic marine (blue), polluted marine air from over Europe (red), African coastal (green) and Saharan dust (brown). The middle two panels show the five-minute averaged [OH] (black dots) and four-minute averaged [HO_2] (blue dots), respectively. The bottom panels show the supporting measurements of $J(O^1D)$ (red line), O_3 (blue dots), CO (green dots), NO (black dots) and NO_2 (dark yellow dots) for each 5-min HO_x-data point. It should be

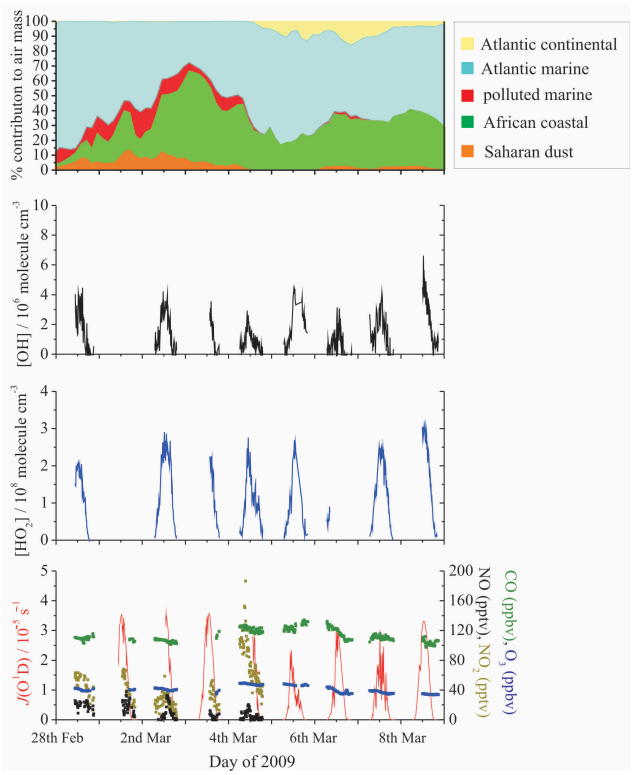

Fig. 3. Time-series of OH, HO_2 and supporting measurements for SOS1. Top panel: source-region percentage contributions to air mass from Atlantic continental (yellow area), Atlantic marine (blue area), polluted marine (red area), African coastal (green area) and Saharan dust (brown area). Middle panels: observed concentrations of OH (five-minute average) and HO_2 (four-minute average). Bottom panel: five-minute averaged $J(O^1D)$ (red line), and the average mixing ratios of CO (green dots), O_3 (blue dots), NO (black dots) and NO_2 (dark yellow dots); for clarity only the supporting data that are simultaneous with HO_x-measurements are shown.

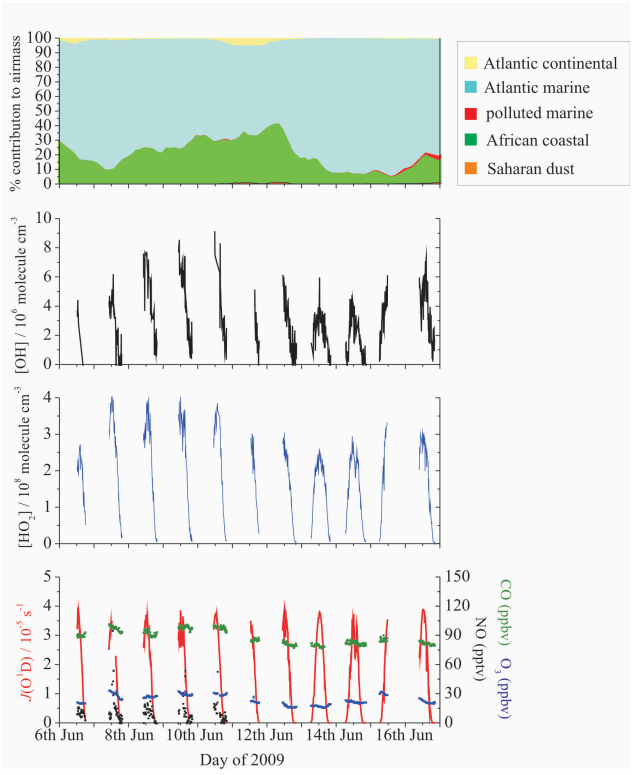

Fig. 4. Time-series of OH, HO_2 and supporting measurements for SOS2. Top panel: source-region percentage contributions to air mass from Atlantic continental (yellow area), Atlantic marine (blue area), polluted marine (red area), African coastal (green area) and Saharan dust (brown area). Middle panels: observed concentrations of OH (five-minute average) and HO_2 (four-minute average). Bottom panel: five-minute averaged $J(O^1D)$ (red line), and the average mixing ratios of CO (green dots), O_3 (blue dots) and NO (black dots); for clarity only the supporting data that are simultaneous with HO_x-measurements are shown.

noted that gaps in the time-series are either because the measuring instruments were not operational, the meteorological conditions were highly unfavourable during those times (e.g. heavy rainfall, very calm wind or strong wind from the direction of local pollution sources), or the HO_x-data failed certain tolerances (e.g. laser instability, lack of NO flow). There were no measurements of NO_x from 5–8 March, 11–16 June and no data for either NO_x or CO for the whole of SOS3. It can be seen that HO_x was observed for 8, 11 and 14 days for SOS1, 2 and 3, respectively, and that both OH and HO_2 followed clear diurnal cycles.

3.1.1 SOS1 (28 February–8 March 2009)

The conditions during the HO_x-measurements for SOS1 (28 February–8 March) were warm ($T \sim 294$ K) with very little rainfall. The average relative humidity was ~77 %, corresponding to a concentration of water vapour of $\sim 4.7 \times 10^{17}$ molecule cm^{-3}. Winds were typically northeasterly with speeds greater than 4 m s^{-1}. The air mass had strong contributions from Atlantic marine air and from the African coast for most of SOS1. Polluted marine air, having passed over Europe a few days previously, contributed up to ~20 % of the air mass in the first half of this period. Saharan dust contributed up to 10 % in the first half of the HO_x-measurement period, and Atlantic continental air (having passed over North Africa a few days previously) made similar contributions in the latter half. CO and O_3 were relatively constant at ~110 and ~40 ppbv, respectively, although these levels were ~20 % higher on 4 and 5 March. There were generally clear skies, although conditions were overcast from 4–6 March, as can be seen in the behaviour of $J(O^1D)$. Consequently OH and HO_2 showed more structure in their diurnal profiles on those days compared to the rest of the measurement period. Data were recorded for 27 February and 1 March, but were excluded from the final analysis because there may have been local pollution sources those days.

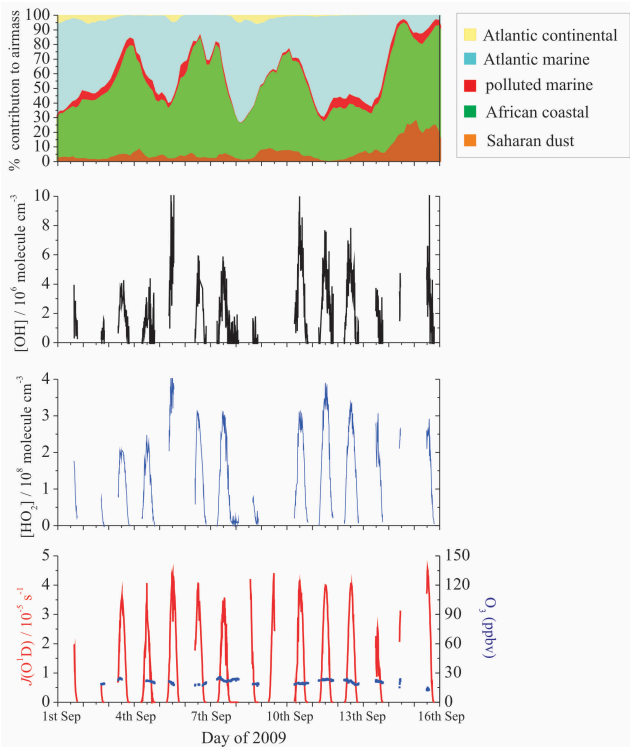

Fig. 5. Time-series of OH, HO_2 and supporting measurements for SOS3. Top panel: source-region percentage contributions to air mass from Atlantic continental (yellow area), Atlantic marine (blue area), polluted marine (red area), African coastal (green area) and Saharan dust (brown area). Middle panels: observed concentrations of OH (five-minute average) and HO_2 (four-minute average). Bottom panel: five-minute averaged $J(O^1D)$ (red line), and the average mixing ratio of O_3 (blue dots); for clarity only the supporting data that are simultaneous with HO_x-measurements are shown.

Very few measurements of [HO_2] were made on 6 March because the supply for the injection of NO was closed to confirm that the cylinder was not in any way a contaminating source of NO at the site.

3.1.2 SOS2 (6–16 June 2009)

The HO_x-measurement period for SOS2 was characterised by warmer ($T \sim 297$ K), with very few periods of cloud cover or rainfall. The mean relative humidity was ~82 %, so that the average concentration of water vapour was $\sim 5.6 \times 10^{17}$ molecule cm^{-3}. As for SOS1, winds were typically north-easterly with speeds more than 4 m s^{-1}. This period experienced the cleanest conditions, with Atlantic marine air as the main source of the sampled air mass for the whole period, although coastal African air contributed up to ~40 % on some days. There was little contribution from polluted marine air, Saharan dust or Atlantic continental air. The noontime peak in $J(O^1D)$ was quite consistent at $\sim 3.7 \times 10^{-5}$ s^{-1} for the whole period. CO and O_3 were higher, at ~100 and ~30 ppbv, respectively, from 7–10 June compared to the rest of SOS2. These dates correspond to the highest peak [OH] and [HO_2] for SOS2 of $\sim 8 \times 10^6$ and $\sim 4 \times 10^8$ molecule cm^{-3}, respectively. From 11 June to the end of SOS2, there was ~80 ppbv of CO and ~20 ppbv of ozone, and the daytime peak [OH] and [HO_2] were relatively constant at $\sim 5 \times 10^6$ and $\sim 2.7 \times 10^8$ molecule cm^{-3}, respectively.

3.1.3 SOS3 (1–15 September 2009)

The meteorological conditions were the most variable during SOS3 with periods of strong daylight interspersed with heavy rainfall, although the temperature remained relatively constant at ~300 K. It was impossible to make HO_x-measurements during the heavy rainfall, which caused flooding at the CVAO, so that there are large gaps in the time-series of [OH] and [HO_2] for those periods. There was also significant electrical power disruption at the site, affecting the ancillary measurements severely – there were no data for NO_x or CO and limited coverage of O_3 and relative humidity. Nevertheless, there were ~211 200 and 169 920 one-second data-points for OH and HO_2, respectively, corresponding to ~700 individual five-minute measurement runs and almost 60 h of HO_x-observations. Winds were typically north-easterly and above 4 m s^{-1} from 1st to 4th, with the relative humidity ~85 % (~4.7×10^{17} molecule cm^{-3} of water vapour). The daytime peak concentrations of OH and HO_2 for these days were $\sim 4 \times 10^6$ and $\sim 2 \times 10^8$ molecule cm^{-3}, respectively. The conditions at the site were very different on the 5th. The relative humidity ranged from a maximum of 89 % in the morning to a minimum of 69 % at 03:00 p.m. local time. Also, the wind swirled at speeds below 2 m s^{-1}, which led to the HO_x instrument sampling air from the exhaust of the generator. Fast conversion of ambient HO_2 to OH by NO led to observations of [OH] exceeding 10^8 molecule cm^{-3}. Measurements where such chemical influence was obvious – over half the data from that day – were excluded from the final analysis, but the remaining data after filtering suggested higher concentrations of OH and HO_2 compared to the rest of SOS3. From the 6th–8th, the north-easterly winds at speeds more than 4 m s^{-1} returned and the relative humidity was again typically ~85 %, and there is good data coverage for those days – the peak daytime concentrations of OH and HO_2 were about 2.5×10^6 and 3×10^8 molecule cm^{-3}, respectively. An almost full night of measurements of [OH] and [HO_2] was made from 7th–8th, the only time possible during the whole SOS; the observations for this night will be discussed further in the following sections. There was then a marked change in the relative humidity at the site. The concentration of water vapour from 1st to 9th was in the range 7–8 $\times 10^{17}$ molecule cm^{-3}, compared to 6–7 $\times 10^{17}$ molecule cm^{-3} (relative humidity ~75 %) for 10th–12th. The skies were generally clear, and the daytime peak [OH] and [HO_2] were in the ranges 6–10 $\times 10^6$

and 3–4 × 10^8 molecule cm^{-3}, respectively. The wind speed dropped below 2 m s^{-1} in the late afternoon of the 12th and remained low through the 13th, similar to the conditions of the 5th, with the relative humidity rising to ∼92 %. However, there was no evidence of ambient HO_2-OH conversion. Heavy rainfall again prevented measurements of OH and HO_2 on the 14th and most of the 15th.

3.2 Seasonal behaviour

Figure 6 shows the median half-hourly averaged diurnal profiles of OH, HO_2 and P(OH) for SOS. The error bars represent the 1σ day-to-day variability in the half-hour averaged data and, although the diurnal profiles for the three measurement periods do agree within the combined 1σ limits, the data around local noon (i.e. 10:00 to 14:00) for SOS1 is statistically different (at 95 % confidence limit of a Student's t-test) to the data in the same timeframe for both SOS2 and 3. The peak values of both [OH] and [HO_2] followed the trend SOS1 < SOS2 ∼ SOS3, consistent with the trends in $J(O^1D)$ and water vapour concentration. Similar qualitative trends were observed for the sum of [HO_2] and [RO_2] recorded by the University of Leicester's PERCA instrument (see Carpenter et al., 2010). However, P(OH) appears to follow the opposite trend (i.e. SOS1 > SOS2 ∼ SOS3) because the decrease in [O_3] from SOS1 is larger than the combined increases in $J(O^1D)$ and water vapour concentration. Possible reasons for this discrepancy will be discussed in Sect. 4.1.

The median ratio [HO_2]/[OH] around local noon (10:00 to 14:00) was ∼75 for all three periods. During daylight, it may be expected for this ratio to vary inversely with [NO] because of conversion of HO_2 to OH via Reaction (R4). Simultaneous coverage of [NO] (15 min averaging), [HO_2] and [OH] was limited to only 22 % of the total HO_x coverage – 4 days in SOS1, 5 days in SOS2, with no NO_x measurements in SOS3. Nevertheless, by taking half-hour averages of concurrent [NO], [OH] and [HO_2] between 08:00 and 17:00, it was found that [HO_2]/[OH] was ∼112 in air containing less than 5 pptv of NO and ∼74 for greater than 5 pptv of NO. This trend is consistent with behaviour observed in other environments (e.g. Carslaw et al., 2001; Creasey et al., 2002; Kanaya et al., 2001b), although it must be noted that the dataset in this case is limited to only 92 half-hour averages.

4 Discussion

4.1 Dependence of [OH] and [HO_2] on $J(O^1D)$ and P(OH)

Figures 7 and 8 show [OH] and [HO_2] as functions of $J(O^1D)$ and P(OH) for each of the three measurement periods. Data from SOS1–3 are represented by black, red and green dots, respectively, and the blue lines represent the results of the non-linear fits

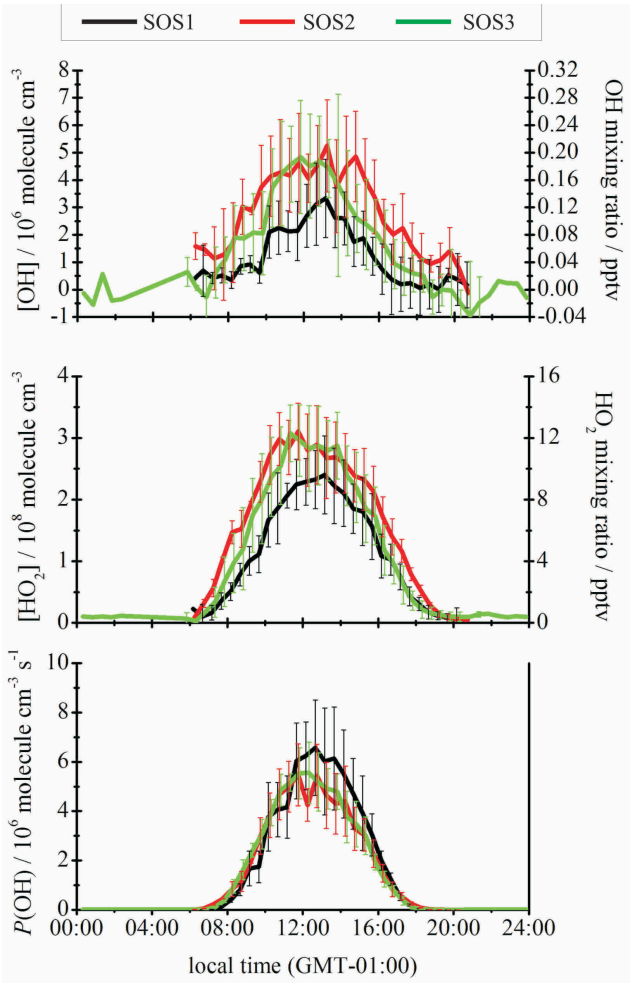

Fig. 6. Half-hourly averaged median diurnal profiles of OH (top panel), HO_2 (middle panel) and primary production rate of OH, P(OH) (bottom panel); SOS1–3 are represented by the black, red and green lines, respectively. The error bars represent the 1σ day-to-day variability of the data.

$$[\text{OH or } HO_2] = a \times (J(O^1D) \text{ or } P(\text{OH}))^b + c \quad (13)$$

to the whole dataset. Tables 3 and 4 show the results of forced fits of Eq. (13) to the observations (i.e. where [OH] is set to a linear relation ($b = 1$) and [HO_2] is set to a square-root relation ($b = 0.5$) – as predicted by the simple steady-state Eqs. (4) and (7), respectively, – and a and c are allowed to vary), with the results of floating fits (i.e. a, b and c allowed to vary) given in parentheses. For clarity, only the standard errors in b for the floating fits are shown, and it can be seen that the values of b from the forced and unforced fits to each dataset do not necessarily agree within error. This disagreement suggests deviations from the simple approach used here caused by, for example, the reactions of HO_2 with O_3 or the photolysis of HO_x-precursors other than ozone, or

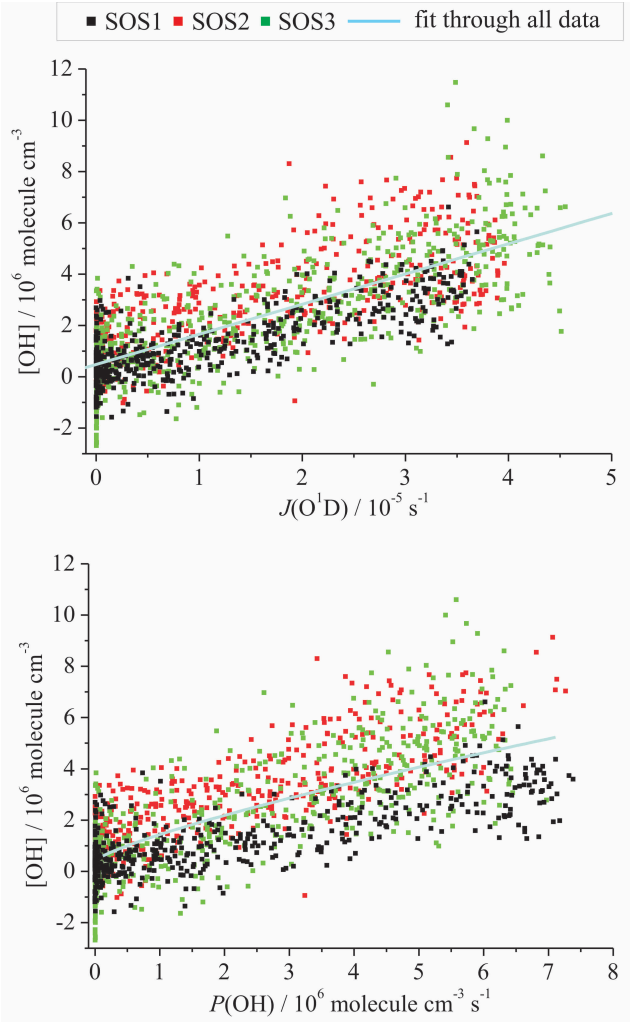

Fig. 7. Plots of five-minute averaged [OH] as a function of $J(O^1D)$ (upper) and $P(OH)$ (lower). Data from SOS1–3 are represented by black, red and green squares, respectively, and the blue lines are the results of the non-linear fits to the complete datasets.

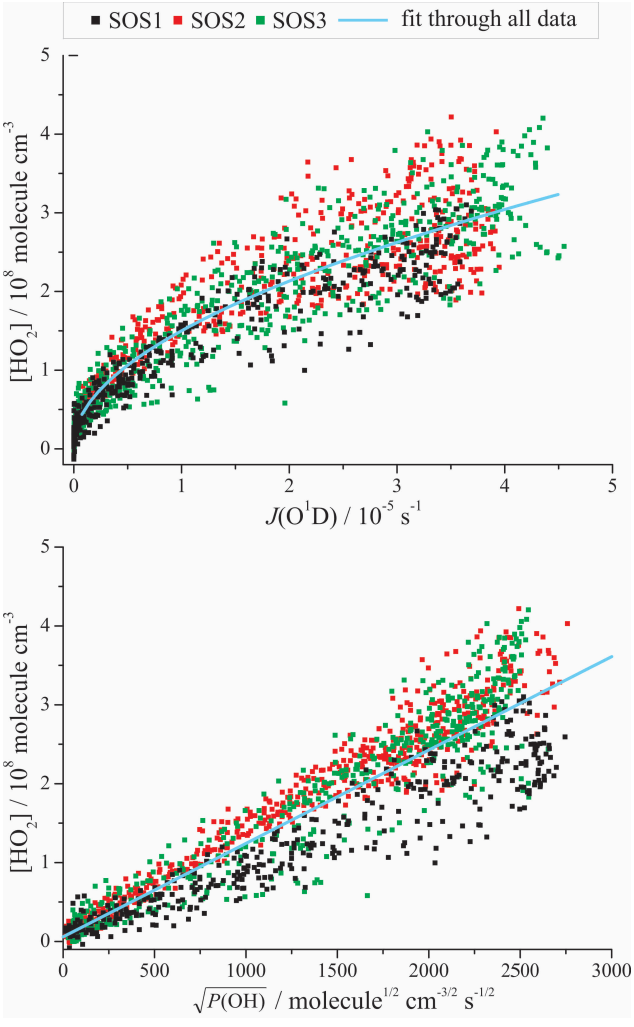

Fig. 8. Plots of four-minute averaged $[HO_2]$ as a function of $J(O^1D)$ (upper) and $P(OH)$ (lower). Data from SOS1–3 are represented by black, red and green squares, respectively, and the blue lines are the results of the non-linear fits to the complete datasets.

a change in the relative importance of HO_x-sinks. It is worth noting that the values of R^2 were virtually the same for the two types of fitting conditions. For ease of comparison with other studies, the following discussion will focus only on the results of the forced fits.

The results show that $[HO_2]$ has excellent correlations with $\sqrt{J(O^1D)}$ and $\sqrt{P(OH)}$, for each measurement period ($R^2 = 0.88$–0.95) and the whole SOS ($R^2 = 0.88$ and 0.87, respectively), suggesting that ~90 % of the variability of that species can be explained by a balance between its production from the reaction of OH and CO and its loss through self-reaction and reaction with CH_3O_2. These results also imply that the behaviour of HO_2 at the CVAO can be broadly described by the equations

$$[HO_2]/\text{molecule cm}^{-3} = 4.7 \times 10^{10} \times \sqrt{J(O^1D)/\text{s}^{-1}} \quad (14)$$

$$[HO_2]/\text{molecule cm}^{-3} = 1.2 \times 10^5 \times \sqrt{P(OH)/\text{molecule cm}^{-3}\,\text{s}^{-1}} \quad (15)$$

A linear fit of $[HO_2]$ to $\sqrt{P(OH)\tau_{OH}}$ (see Eq. 7), where τ_{OH} is the lifetime of OH for each individual SOS campaign calculated from the linear fit of [OH] to $P(OH)$, improves the correlation coefficient slightly ($R^2 = 0.93$). There is no further improvement in R^2 when relating $[HO_2]$ to $\sqrt{P(OH)\tau_{OH}[CO]}$.

[OH] correlates less well than $[HO_2]$ with both $J(O^1D)$ and $P(OH)$, and in fact it appears that the entire [OH] dataset

Table 3. Results of the analytical fits of Eq. (13) for $J(O^1D)$ to the observed five-minute averaged [OH] and four-minute averaged [HO_2]. The units of a are molecule cm^{-3} s (for $b=1$) and molecule cm^{-3} $s^{1/2}$ (for $b=0.5$), for OH and HO_2, respectively. The units of c are molecule cm^{-3}. For ease of comparison, the values displayed in bold are those for forced fits of $b=1$ and $b=0.5$ for [OH] and [HO_2], respectively; the values in parentheses are the results of unforced fits together with the standard errors on b. The values of R2 are virtually the same for the respective forced and unforced fits.

	OH				HO_2			
	$a/10^{11}$	b	$c/10^6$	R^2	$a/10^{10}$	b	$c/10^6$	R^2
SOS1	**0.90**	**1** (*1.36 ± 0.12*)	**0.39** (0.46)	**0.62**	**4.10**	**0.5** (*0.54 ± 0.02*)	**5.6** (10.6)	**0.90**
SOS2	**1.09**	**1** (*0.71 ± 0.08*)	**1.18** (0.91)	**0.56**	**4.76**	**0.5** (*0.42 ± 0.02*)	**11.8** (-3.8)	**0.88**
SOS3	**1.30**	**1** (*0.91 ± 0.07*)	**0.25** (0.17)	**0.64**	**4.88**	**0.5** (*0.58 ± 0.02*)	**−0.3** (9.3)	**0.90**
All data	**1.19**	**1** (*0.98 ± 0.05*)	**0.48** (0.50)	**0.59**	**4.72**	**0.5** (*0.53 ± 0.02*)	**3.4** (7.5)	**0.88**

Table 4. Results of the analytical fits of Eq. (13) to the observed five-minute averaged [OH] and four-minute averaged [HO_2] using $P(OH)$. The units of a are s (for $b=1$) and molecule$^{1/2}$ $cm^{-3/2}$ $s^{1/2}$ (for $b=0.5$), for OH and HO_2, respectively. The units of c are 10^6 molecule cm^{-3}. For ease of comparison, the values displayed in bold are those for forced fits of $b=1$ and $b=0.5$ for [OH] and [HO_2], respectively; the values in parentheses are the results of unforced fits together with the standard errors on b. The values of R^2 are virtually the same for the respective forced and unforced fits.

	OH				HO_2			
	a	b	c	R^2	a	b	c	R^2
SOS1	**0.45**	**1** (*1.27 ± 0.13*)	**0.31** (0.44)	**0.59**	**0.91**	**0.5** (*0.55 ± 0.03*)	**5.6** (10.6)	**0.89**
SOS2	**0.82**	**1** (*0.89 ± 0.07*)	**1.10** (1.00)	**0.68**	**1.30**	**0.5** (*0.47 ± 0.02*)	**9.2** (4.5)	**0.95**
SOS3	**0.89**	**1** (*0.88 ± 0.08*)	**0.21** (0.11)	**0.64**	**1.29**	**0.5** (*0.57 ± 0.03*)	**1.1** (9.7)	**0.92**
All data	**0.70**	**1** (*0.79 ± 0.05*)	**0.58** (0.40)	**0.53**	**1.18**	**0.5** (*0.48 ± 0.02*)	**5.9** (3.6)	**0.87**

can be slightly better described by a linear relation with $J(O^1D)$ ($R^2=0.59$) rather than $P(OH)$ ($R^2=0.53$). Similarly, averaging the data across longer time-periods only slightly improves the fit of Eq. (13) to the complete OH dataset. Also, the parameters a, b and c for the raw 5-min data and the increased averaging agree within the standard errors of the fits; for example, two-hour averaging of the OH data results in fit parameters of $b=0.94$ (±0.14), $c=0.43$ (±0.19) $\times 10^6$ molecule cm^{-3} and $R^2=0.62$, where the values in parentheses are the standard errors on the results of the fit. Thus, the fit results to [OH] suggest that 50–70 % of the variability of OH in each measurement period can be explained by the primary production process (R1–R2).

Comparing the three campaigns, the values of a do not agree within the standard errors of the fits (for clarity, these are not shown in Tables 3 and 4) and follow the general trend SOS1 < SOS2 ≤ SOS3 for both OH and HO_2, suggesting that the sources of HO_x are greater and/or the sinks are less in the summer months than in winter. In fact, a is equal to the lifetime of OH for a linear fit of [OH] to $P(OH)$. Thus, the results suggest τ_{OH} in the winter (∼0.45 s) is approximately half that in the summer, implying that the sinks of OH were stronger in SOS1 compared to SOS2 and 3. In terms of the relationship between HO_2 and $P(OH)$ (Eq. 7) in a low-NO_x environment, the parameter a provides information of the mean ratio of [CH_3O_2] to [HO_2], α, i.e.

$$a_{HO_2-P(OH)} = \sqrt{\frac{k_3[CO]}{2k_5+k_7\alpha}} \times \sqrt{\tau} \quad (16)$$

Using average values of [CO] of 2.7 (SOS1) and 2.2 (SOS2) $\times 10^{12}$ molecule cm^{-3} and the rate constants $k_3 = 2.3 \times 10^{-13}$ cm^3 $molecule^{-1}$ s^{-1}, $k_5 = 6.4$ (SOS1) and 6.9 (SOS2) $\times 10^{-12}$ cm^3 $molecule^{-1}$ s^{-1} (the values are different because of the dependence of k_5 on the concentration of water vapour and temperature) and $k_7 = 5.3 \times 10^{-12}$ cm^3 $molecule^{-1}$ s^{-1}, calculated using the recommendations in Atkinson et al. (2004) and Atkinson et al. (2006), provides values of α of ∼4.1 and 2.1 for SOS1 and 2, respectively. These results suggest that HO_2 could constitute up to 20 % of the total budget of peroxy radicals in winter compared to up to a third in the summer, if CH_3O_2 is the dominant organic peroxy radical.

The reason for the trend in concentrations of OH and HO_2 not following the trend in $P(OH)$ is not immediately clear.

One possibility would be that the trend is a result of errors in the field calibrations – for example, the true sensitivity of the instrument for OH and HO_2 during SOS1 would have to be lower than that from derived from the calibration. The instrument was calibrated by observing the signal from known concentrations of OH and HO_2 generated by the photolysis of water at $\lambda = 184.9$ nm using light from a mercury pen-ray lamp. An error or deviation in the calibration of the flux from that lamp would lead to a systematic error in the observed instrument sensitivity. However, two different pen-ray lamps were used in the field, and the results of the instrument calibrations were in good agreement. The field calibrations of the fluxes of these lamps at $\lambda = 184.9$ nm also agreed well with laboratory tests. These observations would suggest that the difference in the trends of [OH], [HO_2] and P(OH) was not a result of errors in the instrument calibration.

The most likely explanation would be that there is seasonality in the sinks of HO_x. Long-term measurements at the CVAO show that there is a tendency in the levels of VOCs to be higher in winter than in summer months, as shown in Table 2 (see also Read et al., 2009; Carpenter et al., 2010), which may explain, to some extent, the lower OH observed in February compared to June and September. However, one would still expect the reactions with methane and CO to be the dominant sinks for OH, and modelling studies suggest that CO represents 36.7 % and 38.1 % of the total OH loss during SOS1 and SOS2, respectively, while CH_4 represents 14.2 % and 18.0 % of the total OH loss during SOS1 and SOS2, respectively. It is known that the export of Saharan dust across the Atlantic Ocean exhibits strong seasonal behaviour (see, for example, Schepanski et al., 2009). In winter, the dust layer is transported within the trade-wind layer in a south-west direction and at near-surface levels, frequently depositing in the region of the Cape Verde archipelago, while in the summer, the dust remains elevated above the boundary layer and is transported westwards (i.e. there is little deposition to Cape Verde). Figures 3–5 show there was a small but significant contribution to the air mass from Saharan dust for SOS1 (up to ∼15 %) and 3 (up to ∼30 %), but little in SOS2. Also, aerosol sampling measurements at the CVAO revealed approximately half the samples were of high mass concentration (i.e. greater than 60 µg m^{-3}) in the winter months compared to very few (∼5 %) in the summer months (see Carpenter et al., 2010). Whalley et al. (2010) used models to show that heterogeneous loss of HO_2 on aerosols is an important process in this region, constituting ∼23 % of the total loss of HO_2 at noontime and leading to a reduction in daytime HO_2 of ∼30 % compared to the modelled scenario with no aerosol uptake. Those authors also showed that the halogen oxides, IO and BrO, were important instantaneous sinks for HO_2 (∼19 %), despite being present at only a few pptv, and that the combined effects of heterogeneous losses and halogen oxide chemistry reduced modelled daytime HO_2 by ∼50 % compared to the modelled scenario without such processes; it should be noted, however, that the impact on OH was only a few percent. It is conceivable, therefore, that the observed winter-summer trends observed in HO_2 in this study may be influenced by the seasonality of the concentrations of both aerosols and halogen oxides. Unfortunately, no measurements of halogen oxides were possible during SOS. The measurements by Mahajan et al. (2010) at the CVAO in 2007 suggested that the concentrations of both IO and BrO were relatively consistent throughout the year, although Whalley et al. (2010) suggested that the day-to-day variability in their measurements of OH and HO_2 could be explained by variability in concentrations of halogen oxides. A detailed modelling study is required to fully assess the chemical influences on the seasonal behaviour of OH and HO_2, and that will be the focus of a future paper.

4.2 Comparison with other measurements

The levels of OH and HO_2 observed during the SOS are similar to measurements in other clean, remote environments (see Table 1). The maximum concentrations of both species observed here are lower than the highest values reported in polluted tropical locations (Shirley et al., 2006; Dusanter et al., 2009a, b; Hofzumahaus et al., 2009), where the chemical regime is much more complex. The most direct comparison can be made to the 2007 measurements at the CVAO. The measurements of OH and HO_2 during RHaMBLe and SOS2 were taken at roughly the same time of year – late May to early June. Figure 9 shows the hourly-averaged median diurnal profiles of OH, HO_2 and P(OH) for those two campaigns (calculated using the typical values of relative humidity and the mixing ratio of O_3 reported in Whalley et al., 2010). The black lines represent the new dataset, the red lines the 2007 data and the error bars represent the 1σ day-to-day variability in the hourly-averaged data. Instrument problems during the 2007 study meant that only HO_2 was measured for the early part of the campaign, with simultaneous observations of OH and HO_2 possible during the last 5 days, so the solid red line in one-second values for the panel C shows P(OH) when OH was recorded and the dashed line is for when HO_2 was measured. There appears to be reasonably good agreement between the profiles of P(OH) for SOS2 and the 5 days that OH was measured during RHaMBLe, at least before local noon. A Student t-test of the OH data for 10:00–14:00 shows no significant statistical difference between the two campaigns at the 95 % confidence level, despite the limited dataset for OH from RHaMBLe. The hourly-averaged concentrations of HO_2 between 10:00 a.m. and 02:00 p.m. are statistically higher for SOS2 than RHaMBLe (at the 95 % confidence level), although they do agree within the 1σ day-to-day variability. Interestingly, P(OH) was higher for RHaMBLe than SOS2, but levels of NO_x were lower in 2007 than in 2008 and 2009 (see Carpenter et al., 2010), suggesting that sinks for HO_2 such as heterogeneous loss through interaction with aerosols may have been stronger in the 2007 study.

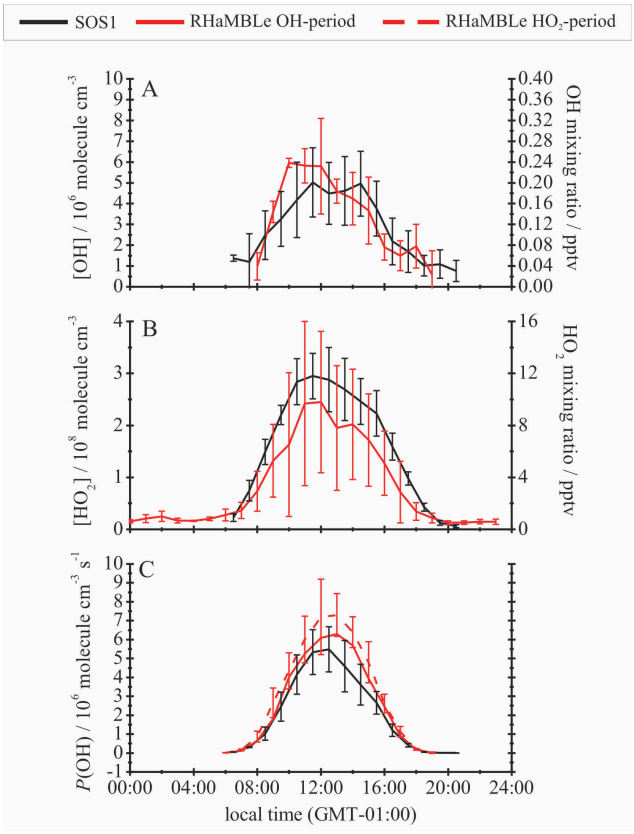

Fig. 9. Plots of the hourly-averaged median diurnal profiles of OH **(A)**, HO_2 **(B)** and P(OH) **(C)** for SOS2 (June 2009; black lines) and RHaMBLe (May–June 2007; solid red OH-measuring period, dashed red HO_2-measuring period). The error bars represent the 1σ day-to-day variability in the hourly-averaged data. For clarity, the error bars on P(OH) for the OH-measuring period are not shown.

It was found that the linear correlation between hourly-averaged values of [OH] and $J(O^1D)$ was poor in 2007 ($a = 1.5 \times 10^{11}$ molecule cm^{-3} s^{-1}, $c = 1.1 \times 10^6$ molecule cm^{-3}, $R^2 = 0.35$ for b set to 1; Furneaux, 2009), although it should be remembered that instrument difficulties led to only 5 days of OH measurements. No assessment of the relationship between [HO_2] and $J(O^1D)$ or P(OH) was made. The ship-based measurements of [OH] over the tropical Atlantic ocean during ALBATROSS correlated quite well with $J(O^1D)$ ($a = 1.4 \times 10^{11}$ molecule cm^{-3} s^{-1}, $c = 0.2 \times 10^6$ molecule cm^{-3}, $R^2 = 0.72$ for b fixed to 1; Brauers et al., 2001). The values of a from these two studies are close the average SOS value, suggesting that the effects of the chemical processing during the three different campaigns – separated by 13 yr – produced similar dependences of [OH] on $J(O^1D)$. By taking an average of the a-values, the contribution to OH in the tropical Atlantic MBL from photolytic processes may be described by the expression

$$[\mathrm{OH}]/\mathrm{molecule\,cm^{-3}} = 1.3 \times 10^{11} \times J(O^1D)/\mathrm{s^{-1}} \quad (17)$$

However, the results shown in Table 3 suggest that there appears to be a seasonal dependence of OH on $J(O^1D)$, so this expression should only be used as a crude approximation when examining the long-term influence of OH in the tropical MBL.

It should be noted that the correlations between [OH] and $J(O^1D)$ in the tropical Atlantic MBL are not as strong as the result of Rohrer and Berresheim's five-year study in rural Germany ($R^2 = 0.88$). Nevertheless, the correlations between [OH] and $J(O^1D)$ in the tropical Atlantic MBL are stronger than those yielded from measurements in tropical forested and urban environments, where the chemical complexity leads to deviations from the simple steady-state approximation. For example, the airborne study over the Suriname rainforest by Martinez et al. (2008) found that correlations of OH with P(OH) and HO_2 with $\sqrt{P(\mathrm{OH})}$were poor in the boundary layer over the forest ($R^2 = 0.19$ and 0.24, respectively), compared to in the boundary layer over the Atlantic ocean and the free troposphere over both regions ($R^2 = 0.47$–0.76). Those authors suggested that the poor correlation over the forest resulted from the recycling of OH through its chemistry with isoprene. In an example of an urban study of tropical OH, Dusanter et al. (2009a) reported that only ~20 % of the variance in OH in Mexico City during MCMA-2006 could be attributed to the variation in J(HONO), and that the correlation between OH and $J(O^1D)$ was worse. Thus, while Eq. (17) may hold reasonably well for OH in the tropical Atlantic MBL, it seems clear that the influence of local chemistry is prohibitive in deriving a uniform expression for the behaviour of [OH] across the tropics.

This work represents the first study of the long-term behaviour of HO_2 and its dependence of $J(O^1D)$ in any environment. The relationship between [HO_2] and the square-roots of both $J(O^1D)$ and P(OH) agrees well with observations in other clean environments. For example, Creasey et al. (2003) found that the slope of a plot of log [HO_2] against log $J(O^1D)$ for one day of baseline conditions (i.e. very low NO, <2 pptv) during SOAPEX was equal to 0.49, compared to a slope of 0.48 for a similar plot of all the HO_2 data in this study. Deviations from the square-root relation have been observed in regions where NO_x chemistry becomes more influential. For instance, Kanaya et al. (2001b) found during ORION99 that the power law dependence of HO_2 on $J(O^1D)$ was $b \sim 0.5$ when NO was below 300 pptv, $b \sim 1$ when NO was more than 1000 pptv, and b was between 0.5 and 1 in the intermediate range of NO. Also, this study at the CVAO has shown that ~90 % of the variability of HO_2 can be explained by $J(O^1D)$ in a remote environment, compared to only 36 % reported by Holland et al. (2003) for a site in rural Germany, where levels of NO were significant (i.e. several ppbv).

4.3 Nighttime measurements of OH and HO_2

Measurements of OH and HO_2 at night (here defined as $J(O^1D) < 10^{-7}\,s^{-1}$, typically before 06:00 a.m. and after 06:00 p.m. local time) were limited, and a prolonged study of nighttime OH and HO_2 was only possible during one night of the SOS – 7 September 2009. The solid black lines in Fig. 10 represent the time-series of OH and HO_2 for that night, the dashed line the respective LODs and the red line represents $J(O^1D)$. It can be clearly seen that HO_2 persists into the night above the LOD, with an average concentration of $\sim 10^7$ molecule cm^{-3}. The values of [OH] for the night of 7 September 2009 are normally distributed about $\sim 8 \times 10^4$ molecule cm^{-3}, with a standard deviation close to the five-minute LOD, suggesting that OH does not persist at measurable levels at least for that night.

Whalley et al. (2010) were not able to perform nighttime measurements of OH at CVAO in 2007, so no comparison can be made. However, they did observe $\sim 10^7$ molecule cm^{-3} of HO_2 at night, similar levels to those observed on the night of 7 September 2009. In fact, the mean concentration of HO_2 when $J(O^1D) < 10^{-7}\,s^{-1}$ was ca. 10^7 molecule cm^{-3} for SOS1–3, above the averaged LOD, suggesting that there was some persistence of HO_2 at night in each of the three measurement periods. It is worth noting that $\Sigma(RO_2 + HO_2)$ was also observed to persist through the night at levels of almost 10 pptv (ca. 2.5×10^8 molecule cm^{-3}) (see Carpenter et al., 2010).

Whalley et al. (2010) observed that HO_2 followed the nighttime profile of O_3, suggesting that entrained air during the night was providing the source of radicals. On the night of 7 September 2009, O_3 remained constant at ~23 ppbv, so it was impossible to identify a link between [HO_2] and ozone levels in this study. Whalley et al. (2010) also suggested that the source was the decomposition of peroxyacetyl nitrate (PAN) and used a box model to show that ~100 pptv of PAN was sufficient to reproduce their nighttime levels of HO_2. Nighttime levels of NO_y, which would include PAN, of the order of hundreds of pptv were measured, so that process may have been an important source of nighttime HO_2 during the SOS.

4.4 Seasonal variance analysis

Rohrer and Berresheim (2006) assessed which factors influenced the variability of OH over five years by calculating the contributions to V_{OH}, the mean of the variances in [OH] divided into a range of timebins. For example, for a 5-yr dataset divided into timebins of 24 h, V_{OH} was calculated as the average of the daily variances of [OH]. Those authors then suggested that this total variance was a combination of three individual variances, such that

$$V_{OH} = (V_{OH} \times R^2(JO^1D)) + V_{inst} + V_{other} \quad (18)$$

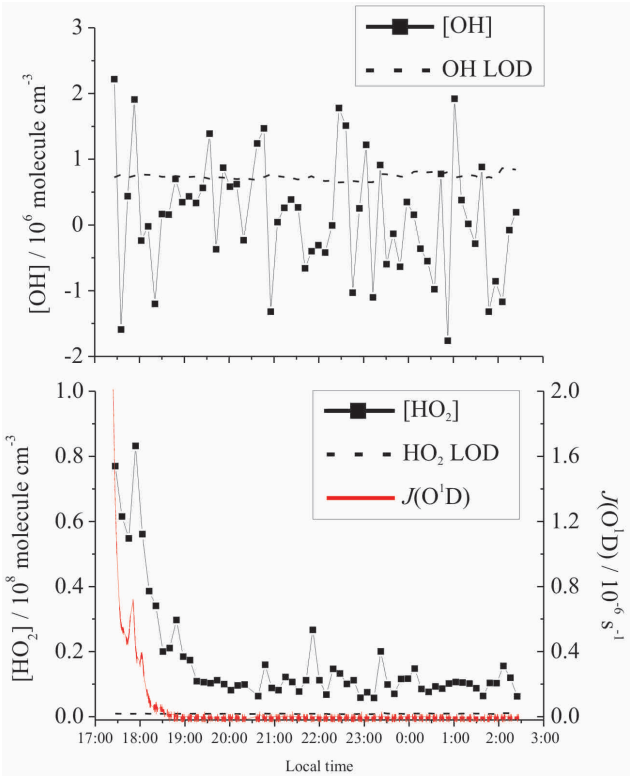

Fig. 10. The time-series of the five-minute averaged [OH] and four-minute averaged [HO_2] (solid black lines) and one-second $J(O^1D)$ (red line) for the night of 7 September 2009; the dashed black lines represents the five-minute and four-minute LODs ($S/N = 1$) for OH and HO_2, respectively.

where the first term in this expression represents the mean variance of OH common to $J(O^1D)$, where $R^2(JO^1D)$ is the square of the correlation coefficient for a power fit of [OH] to $J(O^1D)$ (i.e. Eq. 5), V_{inst} is the mean variance due to instrument noise, and V_{other} is the remaining variance due to other sources, including chemical influences. On subtracting V_{inst} from V_{OH}, Rohrer and Berresheim found that the variance of OH across five years was dominated by the diurnal link to $J(O^1D)$ (76 %) and the seasonal cycle (23 %). It was shown that there was no observable long-term trend, such that there was a strong degree of seasonal stability in the relationship between [OH] and $J(O^1D)$ across the five-year study. This behaviour suggested that competing chemical processes influencing the fit parameters in Eq. (5) were compensating for each other across the seasons. This simple relationship was also shown to better describe the observed [OH] than a detailed chemical mechanism.

The observations of [OH] and [HO_2] at the CVAO during 2009 were treated in a similar fashion and the methodology of the variance analysis is provided in the Appendix. Once the total variances and the contributions due to instrument noise and $J(O^1D)$ were calculated for each timebin, the weighted mean value for each of these three variances across

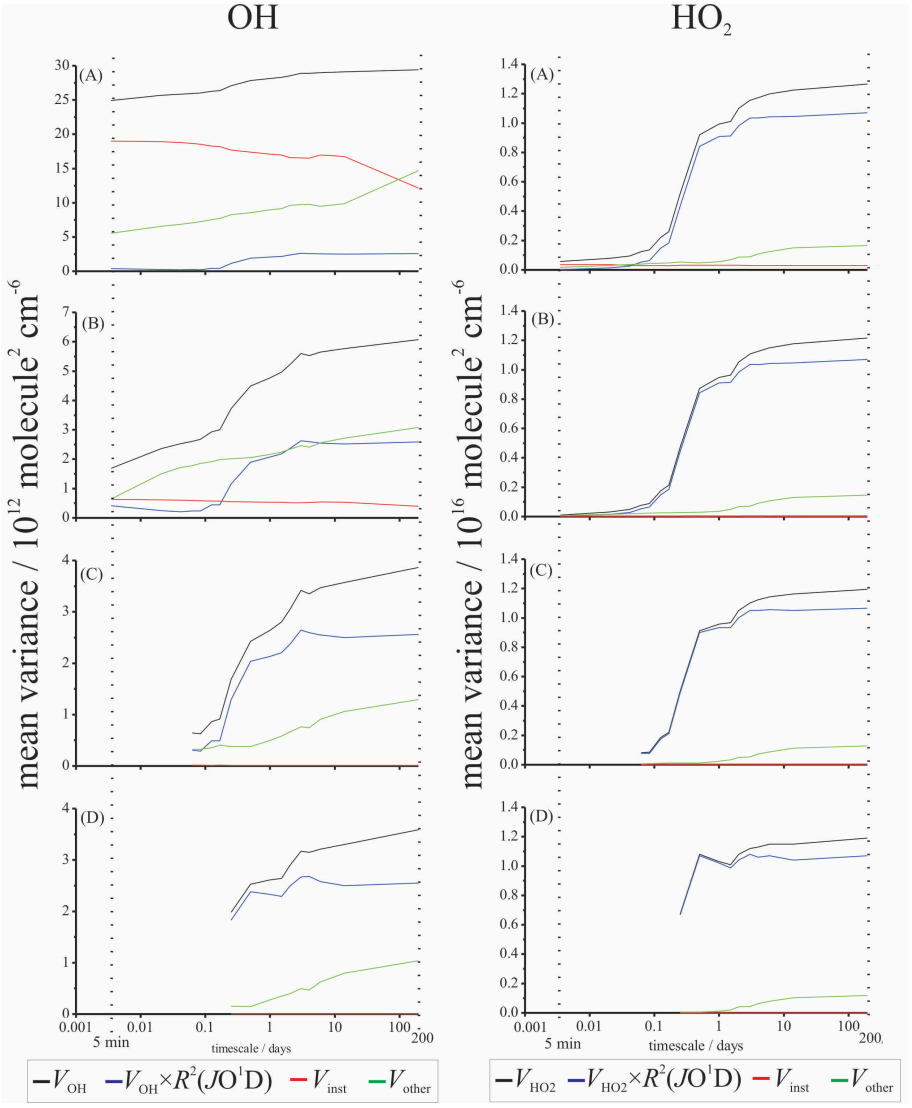

Fig. 11. The mean variances of 1 s **(A)**, 30 s **(B)**, 20 min **(C)** and one hour **(D)** averaged [OH] (left-hand panels) and [HO_2] (right-hand panels) during SOS as a function of binsize; the different coloured lines correspond to the total variance (black), the variance due to instrument noise (red), the variance due to $J(O^1D)$-dependence (blue) and the contribution from other sources (green). The dashed vertical black line represents the timescale of individual measurement runs (i.e. five minutes).

the whole dataset was calculated. The difference between the mean total variance and the sum of the mean variances due to instrument noise and dependence on $J(O^1D)$, is the variance due to unattributed sources, be that from factors influencing instrument noise not accounted for by V_{inst} or chemistry controlling OH and HO_2.

The results of the analysis are shown in Fig. 11. As would be expected, the influence of $J(O^1D)$ becomes more apparent at timebins where its value shows more variation (for instance, above 3 h). The variance of [OH] on a 1 s timescale is dominated by instrument noise (up to 75 % at 5-min binning), unsurprising given that the low concentration of this species leads to fluorescence signals just above the offline signal due to scattered light and dark counts (a 1 s limit of detection for OH would be $\sim 3.5 \times 10^6$ molecule cm^{-3}). This dependence on the instrument noise would also explain the reduced sensitivity of the total variance in 1 s-[OH] to changes in the length of timebin compared to the 1 s-HO_2 data, where the mean total variance in [HO_2] increases by a factor of $\sim$22 from a timescale of 5 min to 200 days (the total number of days spanned from the start of SOS1 to the end of SOS3). The influence of instrument noise on the observed [OH] can be reduced by averaging the 1s-data into 30 s averages, and then binning these calculated means. However, even with prior 30 s-averaging, instrument noise still contributes $\sim$35 % of the observed total variance in [OH] at 5-min and $\sim$6 % at 200

days. Nevertheless, the averaging has now made the temporal variability of [OH] across different timeframes more apparent; for instance, one can now clearly see that the variance in [OH] across a day is a factor of ∼3 more than across 5 min. Averaging across 20 min reduces the contribution of noise further, and it can be seen that the variances tend to more constant values with increasing time-averaging and that the variance of [OH] becomes more clearly controlled by $J(O^1D)$.

The variance due to undefined sources, V_{other}, which includes the variability in the chemical parameters controlling OH and HO_2 other than $J(O^1D)$, gradually increases with timebin-length for OH, but remains relatively constant for timebins greater than 6 days for HO_2, suggesting that timescale as the order of which the air mass is changing. This result may not be unreasonable given the changes in O_3, CO and air mass contribution observed during the SOS (see Figs. 3–5), and is particularly evident for SOS2. The day-to-day diurnal profiles of $J(O^1D)$ were very similar for this period. Figure 4 clearly shows that the levels of OH and HO_2 were relatively constant from 7–10 June, when the mixing ratios of CO and O_3 were also reasonably consistent at ∼100 ppbv and ∼30 ppbv. The air mass was different for the remaining days of SOS2, with a smaller contribution from air originating from the African coast and lower levels of CO and O_3, and the levels of OH and HO_2 are reduced compared to 7th–10th.

After subtracting the effects of instrument noise, the analysis suggests that ∼70 % of the variance of both OH and HO_2 across the SOS can be explained by diurnal behaviour, and about 30 % from changing air mass and seasonal behaviour. It must be remembered that the SOS data are from three short, discrete periods, as opposed to the continuous 5-yr dataset of Rohrer and Berresheim. The sharp rises in variances at the order of 2–3 days may be a result of using a non-continuous dataset containing measurements that were frequently only practical between 06:00 a.m. and 09:00 p.m. local time. Although not shown here, similar variance analysis within each of the three SOS measurement periods showed similar patterns as those seen in Fig. 11. Continuous, long-term measurements at the CVAO would provide better evidence of the existence of any genuine seasonal trends in [OH] and [HO_2] and the relative contributions to the variance in those two species from diurnal and seasonal behaviour.

5 Conclusions

The Leeds aircraft-FAGE system, in its ground configuration, was successfully used to measure the concentrations of OH and HO_2 radicals at the Cape Verde Atmospheric Observatory for a total of 33 days over three periods of 2009 as part of the Seasonal Oxidant Study. This study was the first time that both OH and HO_2 have been measured in a tropical location in order to assess the seasonal variability of these species. The concentrations of both OH and HO_2 followed the trend September ∼ June > February–March, with maximum concentrations of $\sim 9 \times 10^6$ and 4×10^8 molecule cm^{-3}, respectively, observed in the summer months, almost double the observations in winter, when increased levels of dust may act as an enhanced sink for HO_x. The diurnal profiles of the June campaign agreed well with observations at the CVAO two years previously (Whalley et al., 2010). HO_2 was observed to persist into the night at levels of 10^7 molecule cm^{-3}, again consistent with the earlier work of The concentrations of both OH and HO_2 showed good correlations with $J(O^1D)$ and $P(OH)$ were observed, particularly for HO_2, with some differences in behaviour observed for summer and winter months. It was found that ∼60 % and 90 % of the respective variabilities in observed OH and HO_2, respectively, could be described by a simple steady-state approximation based on the primary production of OH from the photolysis of ozone and subsequent reaction of $O(^1D)$ with water vapour. The coefficients yielded from a linear fit of [OH] to $J(O^1D)$ are similar to those yielded from two previous studies in the tropical Atlantic MBL (Whalley et al., 2010; Brauers et al., 2001), possibly suggesting that the behaviour of OH in this region may be predicted using a simple expression. A variance analysis of the data suggested that 30 % of the variance in [OH] and [HO_2] across the study may be attributable to changes in the air mass, although it is recommended that a more complete dataset of observations would lend strength to this conclusion.

The seasonal behaviour of OH observed in this study could have important implications for our understanding of the oxidizing capacity of the Earth's troposphere. However, the observed seasonal trend in OH observed during SOS does not fit with the simple chemistry scheme adopted here. A study of the ability of two atmospheric models to reproduce the observed behaviour in OH and HO_2 – and hence a test of the current understanding of tropospheric chemistry – is the subject of a future paper.

Appendix A

Methodology of variance analysis

Variance analysis was carried out both on the raw one-second dataset and using 30 s, twenty minute and one hour averages. For the averaged data, the values of [OH], [HO_2] and $J(O^1D)$, each recorded at 1 Hz, were grouped into n arrays of length equal to the averaging time in seconds and covering the complete dataset from midnight on 28 February 2009 to midnight on 16 September 2009. Thus, for example, the first such array for the hourly-averaged OH data would contain the OH data between midnight and 01:00 a.m. local time on 28 February 2009 (Julian day 58). Some arrays were excluded from analysis if they did not contain a sufficient number of one-second data – the limits were set at 15, 300 and

900 one-second values for the 30 s, twenty minute and one hour averages, respectively (corresponding to 50 % of a full array for 30 s and 25 % for both 20 min and one hour averaging, a smaller fraction required for the latter two because these averaging times were longer than a typical run time, for which the instrument would only be online for 5 out of ∼8 min). The average values of each of those arrays was calculated and placed in a two-dimensional array that also contained the corresponding average Julian day for each array (t_i) – for example, an hour is ∼0.042 of a day, so that the corresponding array for the hourly-averaged OH data would begin

$$\left\{\begin{array}{l} t_{i=1}, t_{i=2}, t_{i=3}, \ldots\ldots\ldots\ldots\ldots\ldots\ldots\ldots, t_{i=n} \\ \overline{[\mathrm{OH}]}_{i=1}, \overline{[\mathrm{OH}]}_{i=2}, \overline{[\mathrm{OH}]}_{i=3}, \ldots\ldots, \overline{[\mathrm{OH}]}_{i=n} \end{array}\right\} = \left\{\begin{array}{l} 58.021, 58.063, 58.105, \ldots\ldots\ldots \\ \overline{[\mathrm{OH}]}_{i=1}, \overline{[\mathrm{OH}]}_{i=2}, \overline{[\mathrm{OH}]}_{i=3}, \ldots\ldots \end{array}\right\} \quad \text{(A1)}$$

assuming that each of the original arrays contained sufficient one-second data to be included in the analysis.

The timebins that were chosen for the variance analysis were 5 min, 30 min, one hour, 1½ h, 2 h, 3 h, 4 h, 6 h, 12 h, one day, 1½ days, 2 days, 3 days, 4 days, 6 days, 30 days and 200 days. These lengths of timebins were chosen to give the greatest spread in the variability of $J(\mathrm{O^1D})$ – and hence [OH] and [HO_2] – within each timebin (i.e. very little across 5 and 30 min compared to across several hours and days). The timebin of 30 days was chosen so that the average variance would be the average of the variances of each of SOS1–3. The timebin of 200 days was used to calculate the variances across the whole of the SOS.

The variance analysis was carried out on each timebin length sequentially. Thus, the first variance analysis was performed using a timebin of five minutes. The campaign, starting at midnight 28 February 2009 and ending at midnight 16 September 2009, was divided into lengths of time equal to the value of the timebin. For example, there were approximately 57 000 bins of five minutes. The variances of [OH] and [HO_2], V_{OH} and $V_{\mathrm{HO_2}}$, within each timebin were calculated by using the values of the appropriate array (A1) that fall within each timebin. Then, a non-linear fit of the equation

$$[\mathrm{OH}] = (a \times J(\mathrm{O^1D})^{b}) + c \quad \text{(A2)}$$

was made to the data in each timebin, and the R^2 value for that fit was multiplied by the value of V_{OH} or $V_{\mathrm{HO_2}}$ for that timebin. Finally, the variance in [OH] or [HO_2] due to instrument noise, V_{inst}, within each timebin was calculated using the following technique. The values of [OH] and [HO_2] measured at Cape Verde are calculated from

$$\mathrm{HO_x}(t) = \frac{\mathrm{Sig}(t)}{\mathrm{PD}(t) \times C} \quad \text{(A3)}$$

where HO_x represents either OH or HO_2, not the sum of OH and HO_2, Sig(t) is the raw HO_x signal (count s^{-1}) at time t, PD(t) is laser power (mW) and C is the instrument sensitivity (count s^{-1} mW^{-1} cm^3 $molecule^{-1}$). V_{inst}, which is equal to $\sigma^2_{\mathrm{HO_x}}$, can thus be defined by

$$\left(\frac{\sigma_{\mathrm{HO_x}}}{\overline{\mathrm{HO_x}}}\right)^2 = \frac{1}{C^2}\left(\left(\frac{\sigma_{\mathrm{Sig}}}{\overline{\mathrm{Sig}}}\right)^2 + \left(\frac{\sigma_{\mathrm{PD}}}{\overline{\mathrm{PD}}}\right)^2 - \frac{2\sigma_{\mathrm{Sig}}\sigma_{\mathrm{PD}}}{\overline{\mathrm{Sig}} \times \overline{\mathrm{PD}}} R\right) \quad \text{(A4)}$$

where R is the correlation coefficient for a linear fit of PD(t) to Sig(t). The first (signal) term in the large parentheses represents the relative noise of the recorded fluorescence signal. The noise on the signal is defined as shot noise (i.e. $\sigma_{\mathrm{Sig}} = \mathrm{Sig}^{0.5}$), and the total raw signal before correction for background (i.e. total fluorescence + background counts per second) must be used. The second (PD) term in the large parentheses represents the relative noise of the recorded laser power (typically less than 5 %). Thus, Eq. (A4) simplifies to

$$\left(\frac{\sigma_{\mathrm{HO_x}}}{\overline{\mathrm{HO_x}}}\right)^2 = \frac{1}{C^2}\left(\frac{1}{\overline{\mathrm{Sig}}} + \left(\frac{\sigma_{\mathrm{PD}}}{\overline{\mathrm{PD}}}\right)^2 - \frac{2\sigma_{\mathrm{Sig}}\sigma_{\mathrm{PD}}}{\overline{\mathrm{Sig}} \times \overline{\mathrm{PD}}} R\right) \quad \text{(A5)}$$

so that

$$V_{\mathrm{inst}} = \sigma^2_{\mathrm{HO_x}} = \frac{\overline{\mathrm{HO_x}}^2}{C^2} \times \left(\left(\frac{1}{\overline{\mathrm{Sig}}}\right) + \left(\frac{\sigma_{\mathrm{PD}}}{\overline{\mathrm{PD}}}\right)^2 - \frac{2\sigma_{\mathrm{Sig}}\sigma_{\mathrm{PD}}}{\overline{\mathrm{Sig}} \times \overline{\mathrm{PD}}} R\right) \quad \text{(A6)}$$

Therefore, the contribution of instrument noise to the variances in [OH] and [HO_2] can be calculated from this equation for each timebin. If the data are first averaged over x seconds, then the instrument noise is given by

$$\sigma^2_{\mathrm{HO_x}} = \frac{1}{x} \times \frac{\overline{\mathrm{HO_x}}^2}{C^2} \times \left(\left(\frac{1}{\overline{\mathrm{Sig}}}\right) + \left(\frac{\sigma_{\mathrm{PD}}}{\overline{\mathrm{PD}}}\right)^2 - \frac{2\sigma_{\mathrm{Sig}}\sigma_{\mathrm{PD}}}{\overline{\mathrm{Sig}} \times \overline{\mathrm{PD}}} R\right) \quad \text{(A7)}$$

Acknowledgements. The authors would like to thank A. Goddard, P. Edwards and staff in the mechanical and electrical workshops at the School of Chemistry, University of Leeds, for their technical assistance and logistical support throughout the course of this study. We thank R. Leigh of the University of Leicester for providing $J(\mathrm{O^1D})$ data for comparisons of the two radiometers. We would also like to thank B. Faria, L. Mendes and G. Duarte for their logistic assistance in Cape Verde. This project was funded by the NERC (NE/E011403/1), with support of the CVAO by the National Centre for Atmospheric Science (NCAS) and the SOLAS project.

Edited by: A. Hofzumahaus

References

Atkinson, R., Baulch, D. L., Cox, R. A., Crowley, J. N., Hampson, R. F., Hynes, R. G., Jenkin, M. E., Rossi, M. J., and Troe, J.: Evaluated kinetic and photochemical data for atmospheric chemistry: Volume I – gas phase reactions of O_x, HO_x, NO_x and SO_x species, Atmos. Chem. Phys., 4, 1461–1738, doi:10.5194/acp-4-1461-2004, 2004.

Atkinson, R., Baulch, D. L., Cox, R. A., Crowley, J. N., Hampson, R. F., Hynes, R. G., Jenkin, M. E., Rossi, M. J., Troe, J.,

and IUPAC Subcommittee: Evaluated kinetic and photochemical data for atmospheric chemistry: Volume II – gas phase reactions of organic species, Atmos. Chem. Phys., 6, 3625–4055, doi:10.5194/acp-6-3625-2006, 2006.

Bailey, A. E., Heard, D. E., Paul, P. H., and Pilling, M. J.: Collisional quenching of OH ($A\ ^2\Sigma^+$, $\nu\prime = 0$) by N_2, O_2 and CO_2 between 204 and 294 K. Implications for atmospheric measurements of OH by laser-induced fluorescence, J. Chem. Soc., Faraday Trans., 93, 2915–2920, 1997.

Bailey, A. E., Heard, D. E., Henderson, D. A., and Paul, P. H.: Collisional quenching of OH ($A\ ^2\Sigma^+$, $\nu\prime = 0$) by H_2O between 211 and 294 K and the development of a unified model for quenching, Chem. Phys. Lett., 302, 132–138, 1999.

Berresheim, H., Plass-Dülmer, C., Elste, T., Mihalopoulos, N., and Rohrer, F.: OH in the coastal boundary layer of Crete during MINOS: Measurements and relationship with ozone photolysis, Atmos. Chem. Phys., 3, 639–649, doi:10.5194/acp-3-639-2003, 2003.

Bloss, W. J., Evans, M. J., Lee, J. D., Sommariva, R., Heard, D. E., and Pilling, M. J.: The oxidative capacity of the troposphere: coupling of field measurements of OH and a global chemistry transport model, Faraday Discuss., 130, 425–436, 2005a.

Bloss, W. J., Lee, J. D., Johnson, G. P., Sommariva, R., Heard, D. E., Saiz-Lopez, A., Plane, J. M. C., McFiggans, G., Coe, H., Flynn, M., Williams, P., Rickard A. R., and Fleming, Z. L.: Impact of halogen monoxide chemistry upon boundary layer OH and HO_2 concentrations at a coastal site, Geophys. Res. Lett., 32, L06814, doi:10.1029/2004GL022084, 2005b.

Bohn, B., Corlett, G. K., Gillmann, M., Sanghavi, S., Stange, G., Tensing, E., Vrekoussis, M., Bloss, W. J., Clapp, L. J., Kortner, M., Dorn, H.-P., Monks, P. S., Platt, U., Plass-Dülmer, C., Mihalopoulos, N., Heard, D. E., Clemitshaw, K. C., Meixner, F. X., Prevot, A. S. H., and Schmitt, R.: Photolysis frequency measurement techniques: results of a comparison within the ACCENT project, Atmos. Chem. Phys., 8, 5373–5391, doi:10.5194/acp-8-5373-2008, 2008.

Brauers, T., Hausmann, M., Bister, A., Kraus A., and Dorn, H. P.: OH radicals in the boundary layer of the Atlantic Ocean 1. Measurements by long-path laser absorption spectroscopy, J. Geophys. Res.-Atmos., 106, 7399–7414, 2001.

Cantrell, C. A., Edwards, G. D., Stephens, S., Mauldin, R. L., Zondlo, M. A., Kosciuch, E., Eisele, F. L., Shetter, R. E., Lefer, B. L., Hall, S., Flocke, F., Weinheimer, A., Fried, A., Apel., E, Kondo, Y., Blake, D. R., Blake, N. J., Simpson, I. J., Bandy, A. R., Thornton, D. C., Heikes, B. G., Singh, H. B., Brune, W. H., Harder, H., Martinez, M., Jacob, D. J., Avery, M. A., Barrick, J. F., Sachse, G. W., Olson, J. R., Crawford, J. H., and Clarke, A. D.: Peroxy radical behavior during the Transport and Chemical Evolution over the Pacific (TRACE-P) campaign as measured aboard the NASA P-3B aircraft, J. Geophys. Res., 108, 8797–8817, 2003.

Carpenter, L. J., Fleming, Z. L., Read, K. A., Lee, J. D., Moller, S. J., Hopkins, J., Purvis, R., Lewis, A. C., Müller, K., Heinold, B., Herrmann, H., Wadinga Fomba, K., van Pinxteren, D., Müller, C., Tegen, I., Wiedensohler, A., Müller, T., Niedermeier, N., Achterberg, E. P., Patey, M. D., Kozlova, E. A., Heimann, M., Heard, D. E., Plane, J. M. C., Mahajan, A., Oetjen, H., Ingham, T., Stone, D., Whalley, L., Evans, M., Pilling, M. J., Leigh, R. J., Monks, P. S., Karunaharan, A., Vaughan, S., Tschritter, J., Pöhler, D., Frieß, U., Holla, R., Mendes, L., Lopez, H., Faria, B., Manning, A. J., and Wallace, D. W. R.: Seasonal characteristics of tropical marine boundary layer air measured at the Cape Verde Atmospheric Observatory, J. Atmos. Chem., 67, 87–140, 2010.

Carslaw, N., Creasey, D. J., Harrison, D., Heard, D. E., Hunter, M. C., Jacobs, P. J., Jenkin, M. E., Lee, J. D., Lewis, A. C., Pilling, M. J., Saunders, S. M., and Seakins, P. W.: OH and HO_2 radical chemistry in a forested region of north-western Greece, Atmos. Environ., 35, 4725–4737, 2001.

Commane, R., Floquet, C. F. A., Ingham, T., Stone, D., Evans, M. J., and Heard, D. E.: Observations of OH and HO_2 radicals over West Africa, Atmos. Chem. Phys., 10, 8783–8801, doi:10.5194/acp-10-8783-2010, 2010.

Creasey, D. J., Heard, D. E., and Lee, J. D.: Eastern Atlantic Spring Experiment 1997 (EASE97) 1. Measurements of OH and HO_2 concentrations at Mace Head, Ireland, J. Geophys. Res., 107, 4091, doi:10.1029/2001JD000892, 2002.

Creasey, D. J., Evans, G. E., Heard, D. E., and Lee, J. D.: Measurements of OH and HO_2 concentrations in the southern Ocean marine boundary layer, J. Geophys. Res, 108, 4475, doi:10.1029/2002JD003206, 2003.

Davis, D., Grodzinsky, G., Chen, G., Crawford, J., Eisele, F., Mauldin, L., Tanner, D., Cantrell, C., Brune, W., Tan, D., Faloona, I., Ridley, B., Montzka, D., Walega, J., Grahek, F., Sandholm, S., Sachse, G., Vay, S., Anderson, B., Avery, M., Heikes, B., Snow, J., O'Sullivan, D., Shetter, R., Lefer, B., Blake, D., Blake, N., Carroll, M., and Wang, Y.: Marine latitude/altitude OH distributions: Comparison of Pacific Ocean observations with models, J. Geophys. Res.-Atmos., 106, 32691–32707, 2001.

Dorn, H.-P., Neuroth, R., and Hofzumahaus, A.: Investigation of OH absorption cross sections of rotational transitions in the $A^2\sum^+$, (υ'=0)←$X^2\Pi$, (υ''=0) band under atmospheric conditions: Implications for tropospheric long-path absorption measurements, J. Geophys. Res.-Atmos., 100, 7397–7409, 1995.

Dusanter, S., Vimal, D., Stevens, P. S., Volkamer, R., and Molina, L. T.: Measurements of OH and HO_2 concentrations during the MCMA-2006 field campaign – Part 1: Deployment of the Indiana University laser-induced fluorescence instrument, Atmos. Chem. Phys., 9, 1665–1685, doi:10.5194/acp-9-1665-2009, 2009a.

Dusanter, S., Vimal, D., Stevens, P. S., Volkamer, R., Molina, L. T., Baker, A., Meinardi, S., Blake, D., Sheehy, P., Merten, A., Zhang, R., Zheng, J., Fortner, E. C., Junkermann, W., Dubey, M., Rahn, T., Eichinger, B., Lewandowski, P., Prueger, J., and Holder, H.: Measurements of OH and HO_2 concentrations during the MCMA-2006 field campaign – Part 2: Model comparison and radical budget, Atmos. Chem. Phys., 9, 6655–6675, doi:10.5194/acp-9-6655-2009, 2009b.

Ehhalt, D. H. and Rohrer, F.: Dependence of the OH concentration on solar UV, J. Geophys. Res.-Atmos., 105, 3565–3571, 2000.

Eisele, F. L., Tanner, D. J., Cantrell, C. A., and Calvert, J. G.: Measurements and steady state calculations of OH concentrations at Mauna Loa Observatory, J. Geophys. Res.-Atmos., 101, 14665–14679, 1996.

Eisele, F. L., Mauldin, R. L., Tanner, D. J., Cantrell, C., Kosciuch, E., Nowak, J. B., Brune, B., Faloona, I., Tan, D., Davis, D. D., Wang, L., and Chen, G.: Relationship between OH measurements on two different NASA aircraft during PEM Tropics B, J. Geophys. Res.-Atmos., 106, 32683–32689, 2001.

Eisele, F. L., Mauldin, L., Cantrell, C., Zondlo, M., Apel, E., Fried, A., Walega, J., Shetter, R., Lefer, B., Flocke, F., Weinheimer, A., Avery, M., Vay, S., Sachse, G., Podolske, J., Diskin, G., Barrick, J. D., Singh, H. B., Brune, W., Harder, H., Martinez, M., Bandy, A., Thornton, D., Heikes, B., Kondo, Y., Riemer, D., Sandholm, S., Tan, D., Talbot, R., and Dibb, J.: Summary of measurement intercomparisons during TRACE-P, J. Geophys. Res.-Atmos., 108, 8791–8810, 2003.

Emmons, L. K., Apel, E. C., Lamarque, J.-F., Hess, P. G., Avery, M., Blake, D., Brune, W., Campos, T., Crawford, J., DeCarlo, P. F., Hall, S., Heikes, B., Holloway, J., Jimenez, J. L., Knapp, D. J., Kok, G., Mena-Carrasco, M., Olson, J., O'Sullivan, D., Sachse, G., Walega, J., Weibring, P., Weinheimer, A., and Wiedinmyer, C.: Impact of Mexico City emissions on regional air quality from MOZART-4 simulations, Atmos. Chem. Phys., 10, 6195–6212, doi:10.5194/acp-10-6195-2010, 2010.

Forster, P., Ramaswamy, V., Artaxo, P., Berntsen, T., Betts, R., Fahey, D. W., Haywood, J., Lean, J., Lowe, D. C., Myhre, G., Nganga, J., Prinn, R., Raga, G., Schulz, M., and Van Dorland, R.: Changes in Atmospheric Constituents and in Radiative Forcing, in: Climate Change 2007: The Physical Science Basis. Contribution of Working Group I to the Fourth Assessment Report of the Intergovernmental Panel on Climate Change, edited by: Solomon, S., Qin, D., Manning, M., Chen, Z., Marquis, M., Averyt, K. B.,Tignor, M., and Miller, H. L., Cambridge University Press, Cambridge, United Kingdom and New York, NY, USA, 2007.

Fuchs, H., Bohn, B., Hofzumahaus, A., Holland, F., Lu, K. D., Nehr, S., Rohrer, F., and Wahner, A.: Detection of HO_2 by laser-induced fluorescence: calibration and interferences from RO_2 radicals, Atmos. Meas. Tech., 4, 1209–1225, doi:10.5194/amt-4-1209-2011, 2011.

Furneaux, K. L.: Field Studies of the Chemistry of Free-Radicals in the Troposphere using Laser-Induced Fluorescence Spectroscopy, PhD thesis, 2009.

German, K. R.: Direct measurement of the radiative lifetimes of the $A\ ^2\Sigma^+$ ($V\prime = 0$) states of OH and OD, J. Chem. Phys., 62, 2584–2587, 1975.

Heard, D. E. and Pilling, M. J.: Measurement of OH and HO_2 in the Troposphere, Chem. Rev., 103, 5163–5198, 2003.

Hewitt, C. N., Lee, J. D., MacKenzie, A. R., Barkley, M. P., Carslaw, N., Carver, G. D., Chappell, N. A., Coe, H., Collier, C., Commane, R., Davies, F., Davison, B., DiCarlo, P., Di Marco, C. F., Dorsey, J. R., Edwards, P. M., Evans, M. J., Fowler, D., Furneaux, K. L., Gallagher, M., Guenther, A., Heard, D. E., Helfter, C., Hopkins, J., Ingham, T., Irwin, M., Jones, C., Karunaharan, A., Langford, B., Lewis, A. C., Lim, S. F., MacDonald, S. M., Mahajan, A. S., Malpass, S., McFiggans, G., Mills, G., Misztal, P., Moller, S., Monks, P. S., Nemitz, E., Nicolas-Perea, V., Oetjen, H., Oram, D. E., Palmer, P. I., Phillips, G. J., Pike, R., Plane, J. M. C., Pugh, T., Pyle, J. A., Reeves, C. E., Robinson, N. H., Stewart, D., Stone, D., Whalley, L. K., and Yin, X.: Overview: oxidant and particle photochemical processes above a south-east Asian tropical rainforest (the OP3 project): introduction, rationale, location characteristics and tools, Atmos. Chem. Phys., 10, 169–199, doi:10.5194/acp-10-169-2010, 2010.

Hoell, J. M., Davis, D. D., Liu, S. C., Newell, R., Shipham, M., Akimoto, H., McNeal, R. J., Bendura, R. J., and Drewry, J. W.: Pacific Exploratory Mission-West A (PEM-West A): September–October 1991, J. Geophys. Res.-Atmos., 101, 1641–1653, 1996.

Hoell, J. M., Davis, D. D., Jacob, D. J., Rodgers, M. O., Newell, R. E., Fuelberg, H. E., McNeal, R. J., Raper, J. L., and Bendura, R. J.: Pacific Exploratory Mission in the tropical Pacific: PEM-Tropics A, August–September 1996, J. Geophys. Res.-Atmos., 104, 5567–5583, 1999.

Hofzumahaus, A., Rohrer, F., Lu, K. D., Bohn, B., Brauers, T., Chang, C. C., Fuchs, H., Holland, F., Kita, K., Kondo, Y., Li, X., Lou, S. R., Shao, M., Zeng, L. M., Wahner, A., and Zhang, Y. H.: Amplified Trace Gas Removal in the Troposphere, Science, 324, 1702–1704, 2009.

Holland, F., Hofzumahaus, A., Schäfer, J., Kraus, A., and Pätz, H.-W., Measurements of OH and HO_2 radical concentrations and photolysis frequencies during BERLIOZ, J. Geophys. Res.-Atmos., 108, 8246–8267, 2003.

Hosaynali Beygi, Z., Fischer, H., Harder, H. D., Martinez, M., Sander, R., Williams, J., Brookes, D. M., Monks, P. S., and Lelieveld, J.: Oxidation photochemistry in the Southern Atlantic boundary layer: unexpected deviations of photochemical steady state, Atmos. Chem. Phys., 11, 8497–8513, doi:10.5194/acp-11-8497-2011, 2011.

Jacob, D. J., Crawford, J. H., Kleb, M. M., Connors, V. S., Bendura, R. J., Raper, J. L., Sachse, G. W., Gille, J. C., Emmons, L., and Heald, C. L.: Transport and Chemical Evolution over the Pacific (TRACE-P) aircraft mission: Design, execution, and first results, J. Geophys. Res.-Atmos., 108, 9000–9018, 2003.

Kanaya, Y. and Akimoto, H.: Direct Measurements of HO_x Radicals in the Marine Boundary Layer: Testing the Current Tropospheric Chemistry Mechanism, The Chemical Record, 2, 199–211, 2002.

Kanaya, Y., Sadanaga, Y., Matsumoto, J., Sharma, U. K., Hirokawa, J., Kajii, Y., and Akimoto, H.: Nighttime observation of the HO_2 radical by an LIF instrument at Oki Island, Japan, and its possible origins, Geophys. Res. Lett., 26, 2179–2182, 1999.

Kanaya, Y., Sadanaga, Y., Matsumoto, J., Sharma, U. K., Hirokawa, J., Kajii, Y., and Akimoto, H.: Daytime HO_2 concentrations at Oki Island, Japan, in summer 1998: Comparison between measurement and theory, J. Geophys. Res.-Atmos., 105, 24205–24222, 2000.

Kanaya, Y., Matsumoto, J., Kato, S., and Akimoto, H.: Behavior of OH and HO_2 radicals during the Observations atb a Remote Island of Okinawa (ORION99) field campaign. 2. Comparison between observations and calculations, J. Geophys. Res.-Atmos., 106, 24209–24223, 2001a.

Kanaya, Y., Sadanaga, Y., Nakamura, K., and Akimoto, H.: Behavior of OH and HO_2 radicals during the Observations at a Remote Island of Okinawa (ORION99) field campaign. 1. Observation using a laser-induced fluorescence instrument, J. Geophys. Res.-Atmos., 106, 24197–24208, 2001b.

Kanaya, Y., Nakamura, K., Kato, S., Matsumoto, J., Tanimoto, H., and Akimoto, H.: Nighttime variations in HO_2 radical mixing ratios at Rishiri Island observed with elevated monoterpene mixing ratios, Atmos. Environ., 36, 4929–4940, 2002a.

Kanaya, Y., Yokouchi, Y., Matsumoto, J., Nakamura, K., Kato, S., Tanimoto, H., Furutani, H., Toyota, K., and Akimoto, H.: Implications of iodine chemistry for daytime HO_2 levels at Rishiri Island, Geophys. Res. Lett., 29, 1212, doi:10.1029/2001GL014061, 2002b.

Kanaya, Y., Cao, R., Kato, S., Miyakawa, Y., Kajii, Y., Tanimoto, H., Yokouchi, Y., Mochida, M., Kawamura, K., and Akimoto, H.: Chemistry of OH and HO_2 radicals observed at Rishiri Island, Japan, in September 2003: Missing daytime sink of HO_2 and positive nighttime correlations with monoterpenes, J. Geophys. Res.-Atmos., 112, D11308, doi:10.1029/2006JD007987, 2007.

Lawrence, M. G., Jöckel, P., and von Kuhlmann, R.: What does the global mean OH concentration tell us?, Atmos. Chem. Phys., 1, 37–49, doi:10.5194/acp-1-37-2001, 2001.

Lee, J. D., Moller, S. J., Read, K. A., Lewis, A. C., Mendes, L., and Carpenter, L. J.: Year-round measurements of nitrogen oxides and ozone in the tropical North Atlantic marine boundary layer, J. Geophys. Res.-Atmos., 114, D21302, doi:10.1029/2009JD011878, 2009.

Lelieveld, J., Butler, T. M., Crowley, J. N., Dillon, T. J., Fischer, H., Ganzeveld, L., Harder, H., Lawrence, M. G., Martinez, M., Taraborrelli, D., and Williams, J.: Atmospheric oxidation capacity sustained by a tropical forest, Nature, 452, 737–740, 2008.

Mahajan, A. S., Plane, J. M. C., Oetjen, H., Mendes, L., Saunders, R. W., Saiz-Lopez, A., Jones, C. E., Carpenter, L. J., and McFiggans, G. B.: Measurement and modelling of tropospheric reactive halogen species over the tropical Atlantic Ocean, Atmos. Chem. Phys., 10, 4611–4624, doi:10.5194/acp-10-4611-2010, 2010.

Mao, J., Ren, X., Brune, W. H., Olson, J. R., Crawford, J. H., Fried, A., Huey, L. G., Cohen, R. C., Heikes, B., Singh, H. B., Blake, D. R., Sachse, G. W., Diskin, G. S., Hall, S. R., and Shetter, R. E.: Airborne measurement of OH reactivity during INTEX-B, Atmos. Chem. Phys., 9, 163–173, doi:10.5194/acp-9-163-2009, 2009.

Mao, J., Ren, X., Chen, S., Brune, W. H., Chen, Z., Martinez, M., Harder, H., Lefer, B., Rappengluck, B., Flynn, J., and Leuchner, M.: Atmospheric oxidation capacity in the summer of Houston 2006: Comparison with summer measurements in other metropolitan studies, Atmos. Environ., 44, 4107–4115, 2010.

Martinez, M., Harder, H., Kubistin, D., Rudolf, M., Bozem, H., Eerdekens, G., Fischer, H., Klüpfel, T., Gurk, C., Königstedt, R., Parchatka, U., Schiller, C. L., Stickler, A., Williams, J., and Lelieveld, J.: Hydroxyl radicals in the tropical troposphere over the Suriname rainforest: airborne measurements, Atmos. Chem. Phys., 10, 3759–3773, doi:10.5194/acp-10-3759-2010, 2010.

Mauldin, R. L., Tanner, D. J., and Eisele, F. L.: Measurements of OH during PEM-Tropics A, J. Geophys. Res.-Atmos., 104, 5817–5827, 1999.

Mauldin, R. L., Eisele, F. L., Cantrell, C. A., Kosciuch, E., Ridley, B. A., Lefer, B., Tanner, D. J., Nowak, J. B., Chen, G., Wang, L., and Davis, D.: Measurements of OH aboard the NASA P-3 during PEM-Tropics B, J. Geophys. Res.-Atmos., 106, 32657–32666, 2001.

Mauldin, R. L., Cantrell, C. A., Zondlo, M., Kosciuch, E., Eisele, F. L., Chen, G., Davis, D., Weber, R., Crawford, J., Blake, D., Bandy, A., and Thornton, D.: Highlights of OH, H_2SO_4, and methane sulfonic acid measurements made aboard the NASA P-3B during Transport and Chemical Evolution over the Pacific, J. Geophys. Res.-Atmos., 108, 8796–8808, 2003.

Olson, J. R., Crawford, J. H., Davis, D. D., Chen, G., Avery, M. A., Barrick, J. D. W., Sachse, G. W., Vay, S. A., Sandholm, S. T., Tan, D., Brune, W. H., Faloona, I. C., Heikes, B. G., Shetter, R. E., Lefer, B. L., Singh, H. B., Talbot, R. W., and Blake, D. R.: Seasonal differences in the photochemistry of the South Pacific: A comparison of observations and model results from PEM-Tropics A and B, J. Geophys. Res.-Atmos., 106, 32749–32766, 2001.

Olson, J. R., Crawford, J. H., Chen, G., Fried, A., Evans, M. J., Jordan, C. E., Sandholm, S. T., Davis, D. D., Anderson, B. E., Avery, M. A., Barrick, J. D., Blake, D. R., Brune, W. H., Eisele, F. L., Flocke, F., Harder, H., Jacob, D. J., Kondo, Y., Lefer, B. L., Martinez, M., Mauldin, R. L., Sachse, G. W., Shetter, R. E., Singh, H. B., Talbot, R. W., and Tan, D.: Testing fast photochemical theory during TRACE-P based on measurements of OH, HO_2, and CH_2O, J. Geophys. Res.-Atmos., 109, D15S10, doi:10.1029/2003JD004278, 2004.

Pugh, T. A. M., MacKenzie, A. R., Hewitt, C. N., Langford, B., Edwards, P. M., Furneaux, K. L., Heard, D. E., Hopkins, J. R., Jones, C. E., Karunaharan, A., Lee, J., Mills, G., Misztal, P., Moller, S., Monks, P. S., and Whalley, L. K.: Simulating atmospheric composition over a South-East Asian tropical rainforest: performance of a chemistry box model, Atmos. Chem. Phys., 10, 279–298, doi:10.5194/acp-10-279-2010, 2010.

Raper, J. L., Kleb, M. M., Jacob, D. J., Davis, D. D., Newell, R. E., Fuelberg, H. E., Bendura, R. J., Hoell, J. M., and McNeal, R. J.: Pacific Exploratory Mission in the Tropical Pacific: PEM-Tropics B, March-April 1999, J. Geophys. Res.-Atmos., 106, 32401–32425, 2001.

Read, K. A., Mahajan, A. S., Carpenter, L. J., Evans, M. J., Faria, B. V. E., Heard, D. E., Hopkins, J. R., Lee, J. D., Moller, S. J., Lewis, A. C., Mendes, L., McQuaid, J. B., Oetjen, H., Saiz-Lopez, A., Pilling, M. J., and Plane, J. M. C.: Extensive halogen-mediated ozone destruction over the tropical Atlantic Ocean, Nature, 453, 1232–1235, 2008.

Read, K. A., Lee, J. D., Lewis, A. C., Moller, S. J., Mendes, L., and Carpenter, L. J.: Intra-annual cycles of NMVOC in the tropical marine boundary layer and their use for interpreting seasonal variability in CO, J. Geophys. Res.-Atmos., 114, D21303, doi:10.1029/2009JD011879, 2009.

Rohrer, F. and Berresheim, H.: Strong correlation between levels of tropospheric hydroxyl radicals and solar ultraviolet radiation, Nature, 442, 184–187, 2006.

Ryall, D. B., Derwent, R. G., Manning, A. J., Simmonds, P. G., and O'Doherty, S.: Estimating source regions of European emissions of trace gases from observations at Mace Head, Atmos. Environ., 35, 2507–2523, 2001.

Schepanski, K., Tegen, I., and Macke, A.: Saharan dust transport and deposition towards the tropical northern Atlantic, Atmos. Chem. Phys., 9, 1173–1189, doi:10.5194/acp-9-1173-2009, 2009.

Shirley, T. R., Brune, W. H., Ren, X., Mao, J., Lesher, R., Cardenas, B., Volkamer, R., Molina, L. T., Molina, M. J., Lamb, B., Velasco, E., Jobson, T., and Alexander, M.: Atmospheric oxidation in the Mexico City Metropolitan Area (MCMA) during April 2003, Atmos. Chem. Phys., 6, 2753–2765, doi:10.5194/acp-6-2753-2006, 2006.

Singh, H. B., Brune, W. H., Crawford, J. H., Flocke, F., and Jacob, D. J.: Chemistry and transport of pollution over the Gulf of Mexico and the Pacific: spring 2006 INTEX-B campaign overview and first results, Atmos. Chem. Phys., 9, 2301–2318, doi:10.5194/acp-9-2301-2009, 2009.

Smith, S. C., Lee, J. D., Bloss, W. J., Johnson, G. P., Ingham,

T., and Heard, D. E.: Concentrations of OH and HO_2 radicals during NAMBLEX: measurements and steady state analysis, Atmos. Chem. Phys., 6, 1435–1453, doi:10.5194/acp-6-1435-2006, 2006.

Sommariva, R., Haggerstone, A.-L., Carpenter, L. J., Carslaw, N., Creasey, D. J., Heard, D. E., Lee, J. D., Lewis, A. C., Pilling, M. J., and Zádor, J.: OH and HO_2 chemistry in clean marine air during SOAPEX-2, Atmos. Chem. Phys., 4, 839–856, doi:10.5194/acp-4-839-2004, 2004.

Sommariva, R., Bloss, W. J., Brough, N., Carslaw, N., Flynn, M., Haggerstone, A.-L., Heard, D. E., Hopkins, J. R., Lee, J. D., Lewis, A. C., McFiggans, G., Monks, P. S., Penkett, S. A., Pilling, M. J., Plane, J. M. C., Read, K. A., Saiz-Lopez, A., Rickard, A. R., and Williams, P. I.: OH and HO_2 chemistry during NAMBLEX: roles of oxygenates, halogen oxides and heterogeneous uptake, Atmos. Chem. Phys., 6, 1135–1153, doi:10.5194/acp-6-1135-2006, 2006.

Stone, D., Evans, M. J., Commane, R., Ingham, T., Floquet, C. F. A., McQuaid, J. B., Brookes, D. M., Monks, P. S., Purvis, R., Hamilton, J. F., Hopkins, J., Lee, J., Lewis, A. C., Stewart, D., Murphy, J. G., Mills, G., Oram, D., Reeves, C. E., and Heard, D. E.: HO_x observations over West Africa during AMMA: impact of isoprene and NOx, Atmos. Chem. Phys., 10, 9415–9429, doi:10.5194/acp-10-9415-2010, 2010.

Stone, D., Evans, M. J., Edwards, P. M., Commane, R., Ingham, T., Rickard, A. R., Brookes, D. M., Hopkins, J., Leigh, R. J., Lewis, A. C., Monks, P. S., Oram, D., Reeves, C. E., Stewart, D., and Heard, D. E.: Isoprene oxidation mechanisms: measurements and modelling of OH and HO_2 over a South-East Asian tropical rainforest during the OP3 field campaign, Atmos. Chem. Phys., 11, 6749–6771, doi:10.5194/acp-11-6749-2011, 2011.

Tan, D., Faloona, I., Simpas, J. B., Brune, W., Olson, J., Crawford, J., Avery, M., Sachse, G., Vay, S., Sandholm, S., Guan, H.-W., Vaughn, T., Mastromarino, J., Heikes, B., Snow, J., Podolske, J., and Singh, H.: OH and HO_2 in the tropical Pacific: Results from PEM-Tropics B, J. Geophys. Res.-Atmos., 106, 32667–32681, 2001.

Tanner, D. J. and Eisele, F. L.: Present OH measurement limits and associated uncertainties, J. Geophys. Res.-Atmos., 100, 2883–2892, 1995.

Whalley, L. K., Furneaux, K. L., Goddard, A., Lee, J. D., Mahajan, A., Oetjen, H., Read, K. A., Kaaden, N., Carpenter, L. J., Lewis, A. C., Plane, J. M. C., Saltzman, E. S., Wiedensohler, A., and Heard, D. E.: The chemistry of OH and HO_2 radicals in the boundary layer over the tropical Atlantic Ocean, Atmos. Chem. Phys., 10, 1555–1576, doi:10.5194/acp-10-1555-2010, 2010.

Whalley, L. K., Edwards, P. M., Furneaux, K. L., Goddard, A., Ingham, T., Evans, M. J., Stone, D., Hopkins, J. R., Jones, C. E., Karunaharan, A., Lee, J. D., Lewis, A. C., Monks, P. S., Moller, S. J., and Heard, D. E.: Quantifying the magnitude of a missing hydroxyl radical source in a tropical rainforest, Atmos. Chem. Phys., 11, 7223–7233, doi:10.5194/acp-11-7223-2011, 2011.